


Spring 4-6-2017

Simulation and Analysis of a Drilling Fluid Using a Herschel-Bulkley Model

Daniel Powell
University of New Mexico

Follow this and additional works at: https://digitalrepository.unm.edu/me_etds

 Part of the [Computer-Aided Engineering and Design Commons](#), and the [Other Mechanical Engineering Commons](#)

Recommended Citation

Powell, Daniel. "Simulation and Analysis of a Drilling Fluid Using a Herschel-Bulkley Model." (2017).
https://digitalrepository.unm.edu/me_etds/127

This Thesis is brought to you for free and open access by the Engineering ETDs at UNM Digital Repository. It has been accepted for inclusion in Mechanical Engineering ETDs by an authorized administrator of UNM Digital Repository. For more information, please contact disc@unm.edu.

Daniel Powell

Candidate

Mechanical Engineering

This thesis is approved, and it is acceptable in quality and form for publication:

Approved by the thesis committee:

Svetlana Poroseva, Chairperson

Peter Vorobieff

Randall Truman

**SIMULATION AND ANALYSIS OF A DRILLING FLUID USING A
HERSCHEL-BULKLEY MODEL**

by

DANIEL POWELL

**B.S., MECHANICAL ENGINEERING
UNIVERSITY OF NEW MEXICO, 2014**

THESIS

Submitted in Partial Fulfillment of the
Requirements for the Degree of

Master of Science

Mechanical Engineering

The University of New Mexico
Albuquerque, New Mexico

May 2017

DEDICATION

To my daughter, Aria Rose. May your dreams inspire the future.

ACKNOWLEDGEMENTS

I would like to thank my advisor, Dr. Svetlana Poroseva, for all of her guidance through this work. Much of her precious time has gone into the details of this thesis. I appreciate her intention to create excellence, and I will carry that intention into my future work.

I owe much of my interest in the way things work to my father and grandfather. My grandfather taught my dad as he taught me to question the reality we live in. From them, I learned that the greatest question I can ask is, “Why?” I am grateful for instilling in me the confidence to learn and the work ethic to persevere.

I would like to give thanks to my mother for teaching me that life is a series of decisions and that I can create it as I choose.

I am most appreciative of my wife. Without her I surely would have given up. Countless times I said that things were too hard or that I was too tired. She supported me and loved me through it all. She lifted me up and reaffirmed that I would succeed.

Lastly, I would like to thank the Tetra Corporation for funding this work.

**SIMULATION AND ANALYSIS OF A DRILLING FLUID USING A
HERSCHEL-BULKLEY MODEL**

by

Daniel Powell

B.S., Mechanical Engineering, University of New Mexico, 2014

M.S., Mechanical Engineering, University of New Mexico, 2017

ABSTRACT

In the study, a drilling fluid with known properties is analyzed and simulated in the laminar regime through a pipe with dimensions of $1.5m$ in length and $0.02m$ in diameter. The purpose of the conducted analysis is to demonstrate the advantages of the Herschel-Bulkley model currently used in the oil and gas industry for analyzing non-Newtonian drilling fluids.

For comparison, the analysis is also performed using more simple models for non-Newtonian fluids such as the Bingham Plastic model and the Power Law model and for a Newtonian fluid (water). In addition to analytical models, computations are conducted using commercial computational fluid dynamics software: Star-CCM+ and Solidworks Flow Simulation.

The comparison of the model results are mainly considered in the pipe entrance region, because this flow area is of importance for drilling processes. The differences between the fluid models is largely apparent in this region.

TABLE OF CONTENTS

LIST OF FIGURES	viii
LIST OF TABLES	xi
INTRODUCTION	1
FLOW GEOMETRY	4
MATHEMATICAL FRAMEWORK	5
Governing Equations	5
Newtonian Flow Solutions.....	6
Bingham Plastic Flow Solutions.....	13
Power Law Flow Solutions.....	17
Herschel-Bulkley Flow Solutions	18
DRILLING FLUID RHEOLOGY	20
NUMERICAL PROCEDURE	25
Computational Domain and Boundary Conditions.....	25
RESULTS	28
Simulation Convergence for Both Meshes	28
Star-CCM+ Validation using the Analytical Solution of Newtonian Flow	30
Extended Pipe Case for Newtonian Flow	33
Blasius Solution Validation for Newtonian Flow	35
Non-Newtonian Fluid Model Results	39

CONCLUSIONS.....	55
REFERENCES	57

LIST OF FIGURES

Figure 1: Stress/Strain rate curve for fluids [4]	2
Figure 2: Entrance region of modeled pipe.....	4
Figure 3: Pressure vs. flow rate Darley [13].....	15
Figure 4:Fann data and curve fit for Bingham Plastic, Power Law, and Herschel-Bulkley models	21
Figure 5: Residual plots for simulations run in Star-CCM+; a) Fine mesh, b) Coarse mesh.....	29
Figure 6:Star-CCM+ water velocity profile mesh comparison, $x = 0R$ (brown), $x = 2R$ (black), $x = 4R$ (red), $x = 6R$ (magenta), $x = 8R$ (blue), $x = 140R$ (green).....	32
Figure 7: Water velocity profiles for analytical results with a pressure gradient [9] and Star CCM+ results; the color scheme is the same as for Figure 6.....	32
Figure 8: All simulated water velocity profiles; color scheme is the same as in Figure 6	34
Figure 9: Solidworks coarse mesh simulated velocity profile for water in pipe with a length of 1.5m and 2.0m; color scheme is the same as in Figure 6.....	34
Figure 10: Newtonian simulated centerline velocities with approximated centerline velocities [11].....	35
Figure 11: Non-dimensional water velocity profiles for simulated results, zero-pressure gradient, and with pressure gradient analysis [9]; for symbols: $x = 2R$ (o), $x = 4R$ (×), $x = 6R$ (+). $x = 8R$ (*); for solid lines: $x = 2R$ (black), $x = 4R$ (red), $x = 6R$ (blue), $x = 8R$ (magenta) ..	36
Figure 12: Water boundary layer thickness for simulated results, zero-pressure gradient, and with a pressure gradient [9].....	38
Figure 13: Absolute pressure vs volume flow rate for a Bingham Plastic fluid model [15]	40
Figure 14: Critical radius vs differential pressure for a Bingham Plastic fluid [15].....	41

Figure 15: Analytical result for the fully-developed Bingham Plastic velocity profile [15]	41
Figure 16: $x = 2R$ analytical and simulated velocity profiles for Power Law [16], Bingham Plastic [9], and Herschel-Bulkley fluid models	42
Figure 17: $x = 4R$ analytical and simulated velocity profiles for Power Law [16], Bingham Plastic [9], and Herschel-Bulkley fluid models	43
Figure 18: $x = 6R$ analytical and simulated velocity profiles for Power Law [16], Bingham Plastic [9], and Herschel-Bulkley fluid models	43
Figure 19: $x = 8R$ analytical and simulated velocity profiles for Power Law [16], Bingham Plastic [9], and Herschel-Bulkley fluid models	44
Figure 20: $x = 140R$ analytical and simulated velocity profiles for Power Law [9], Bingham Plastic [15], and Herschel-Bulkley [15] fluid models	44
Figure 21: Bingham Plastic simulated centerline velocities with approximated centerline velocities [11].....	48
Figure 22: Power Law simulated centerline velocities with approximated centerline velocities [11].....	48
Figure 23: Herschel-Bulkley simulated centerline velocities with approximated centerline velocities [11].....	49
Figure 24: Non-dimensional analytical [9] and simulated Bingham plastic velocity profiles;for symbols: $x = 2R$ (o), $x = 4R$ (\times), $x = 6R$ (+). $x = 8R$ (*); for solid lines: $x = 2R$ (black), $x = 4R$ (red), $x = 6R$ (blue), $x = 8R$ (magenta).....	50
Figure 25: Non-dimensional analytical [16] and simulated Power Law velocity profiles; symbols and colors are the same as in Figure 24.	51

Figure 26: Herschel-Bulkley simulated and analytical [9] non-dimensional velocity profiles;
symbols and colors are the same as in Figure 24..... 51

Figure 27: a.) Simulated velocity profiles and; b.)Boundary layer thickness comparison for all
three non-Newtonian fluid types; Power Law (dashed lines), Bingham Plastic (dotted lines);
Herschel-Bulkley (solid lines) [9]..... 53

LIST OF TABLES

Table 1: Numerical entrance velocity constants [11]	9
Table 2: Tabulated Blasius solution for laminar flow over a flat plate [9].....	11
Table 3: Measured drilling fluid rheology	20
Table 4: Model coefficients	24
Table 5: Mesh parameters (coarse mesh).....	26
Table 6: Mesh parameters (fine mesh).....	26
Table 7: Flow parameters for water	27
Table 8: Newtonian (water) results.....	31
Table 9: Bingham Plastic fully-developed results	46
Table 10: Power Law fully-developed results	46
Table 11: Herschel-Bulkley fully-developed results	46

INTRODUCTION

The oil and gas industry uses drilling fluids to remove rock cuttings and stabilize the pressure differential at the wellbore wall. The velocity of these fluids is relatively low in certain regions, and the removal of cuttings is accomplished through higher viscosities at lower shear rates. Rheological properties of such fluids, particularly viscosity, are closely monitored and controlled as the fluid is being reprocessed at the top of the well.

To determine the fluid viscosity value, one collects data from a Fann meter for a small sample of drilling fluid and then, post-processes the data using a fluid model. A fluid can be treated as Newtonian, such as water, or non-Newtonian depending on real-life conditions. A difference between Newtonian and non-Newtonian fluids is determined based on the relationship between the shear stress to the shear strain rate. A Newtonian fluid has a linear relation of the shear stress to the shear strain rate and requires no initial stress to begin fluid motion. A non-Newtonian fluid is simply any fluid that behaves in a way contrary to Newtonian behavior.

Models of non-Newtonian fluids can be categorized as Power Law, Bingham Plastic, or Herschel-Bulkley [1]. Other models exist, but they will not be discussed in the thesis as they gained less popularity in the industry. Fluids that have an initial stress required to initiate flow and then have a linear dependence of the shear strain rate to shear stress are Bingham Plastic fluids. Fluids that require no initial shear stress to initiate flow but have a nonlinear stress\strain rate relation are Power Law fluids. Within Power Law fluids there are fluids whose viscosity increases with the rate of shear and those with viscosity that decreases with the rate of shear. These are called ‘shear thickening’ or dilatant and ‘shear thinning’ or pseudo-plastic fluids, respectively [1]. Rarely do non-Newtonian fluids behave exactly according to either of these two

models. Most often fluids exhibit some characteristics of both Power Law and Bingham Plastic fluids. The blend of these two models is the Herschel-Bulkley model. Fluids that obey this model are called Plastic fluids [2]. The Herschel-Bulkley model was first proposed by Winslow Herschel and Ronald Bulkley in an article published in 1926 [3]. A simple graphical depiction of the three non-Newtonian and Newtonian fluid categories is shown in Figure 1.

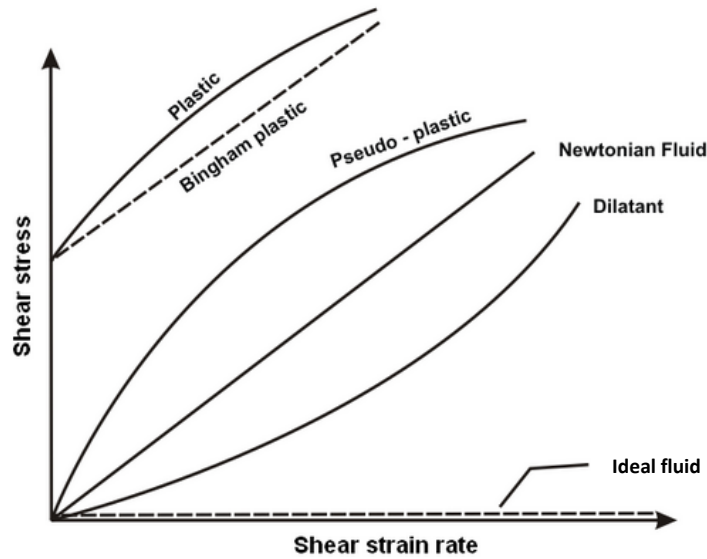


Figure 1: Stress/Strain rate curve for fluids [4]

At the drilling site, the Bingham Plastic or Power Law fluid models are usually used since either model can be derived quickly and the information provides trends in the viscosity of the drilling fluid. However, some drilling fluids do not fit well with either of these models as discussed in the Drilling Fluids Processing Handbook [1]. Specifically, the Power Law and Bingham Plastic models do not accurately capture the shear stress at low shear strain rates as related to viscosity. The errors are apparent at the low shear strain rates and, thus, negatively affect the accuracy of measured viscosity of the drilling fluid. The Herschel-Bulkley model most

accurately portrays the viscosity and is the model commonly used during the engineering process of designing the drilling fluid to a particular application.

The goal of the thesis is to demonstrate the usefulness of the Herschel-Bulkley model when applied to the analysis of a flow of a drilling fluid through a straight circular pipe. The non-Newtonian fluid models are derived experimentally by the methods outlined in the Drilling Fluids Processing Handbook [1]. The model performance will be compared with that of the Power Law and Bingham Plastic models with respect to the boundary layer thickness and the entrance length of a pipe. In the study, a drilling fluid is considered as laminar incompressible non-Newtonian fluid. Also, the results obtained with non-Newtonian models are compared with those for water.

In addition to calculations with analytical models, flow simulations were conducted using commercial software such as Solidworks Flow Simulation [5] and Star-CCM+ [6]. The grid sensitivity analysis was performed using Star-CCM+.

The pressure differential, wall shear stress, and velocity profile were calculated throughout the length of the pipe with each of the fluid models. These flow parameters are important for development of the boundary layer on the pipe wall and the fully-developed pipe flow regime.

The model results will mainly be compared in the pipe entrance region. This flow area is of particular importance for rock cuttings transport. Moreover, the differences between the fluid models are expected to manifest in this region.

FLOW GEOMETRY

In the thesis, the cylindrical coordinate system is used throughout with the r -direction being radial to the pipe and the x -direction being longitudinal to the pipe. The origin is located at the axial center of the pipe with $x = 0$ at the entrance. The pipe has a length $L = 1.5m$ and a diameter $d = 0.02m$. Velocity profiles are sampled at six locations along the pipe: $x = 0.0, 0.02, 0.04, 0.06, 0.08,$ and $1.4 m$. Figure 2 shows a cross section of the pipe modeled in Solidworks. The vertical lines are the positions along the axis where flow characteristics are monitored. At $x = 0$, the flow has uniform velocity in the x -direction.

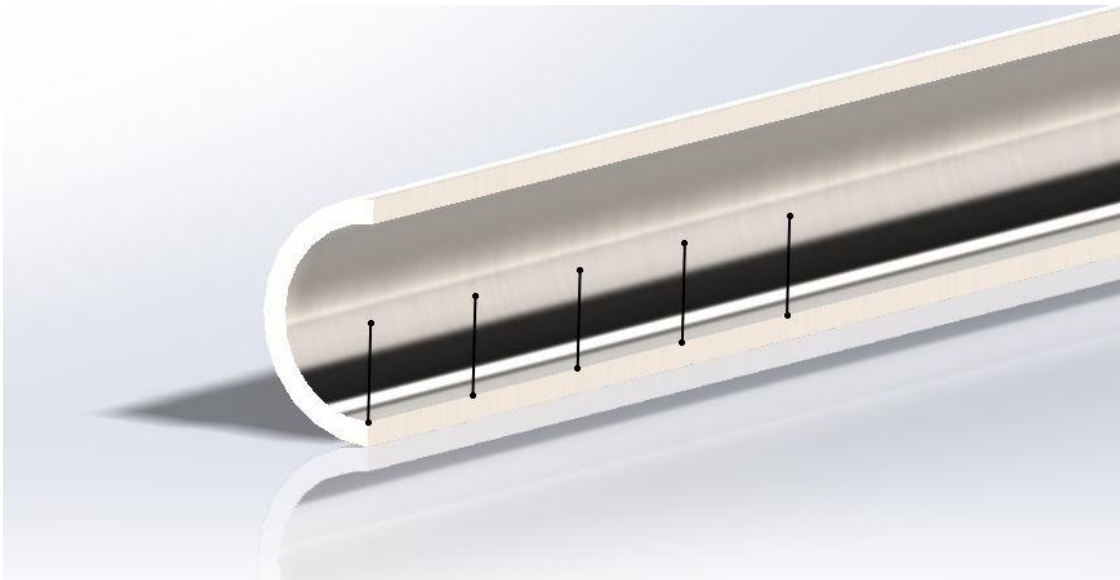


Figure 2: Entrance region of modeled pipe

MATHEMATICAL FRAMEWORK

Governing Equations

The flow is assumed to be steady, incompressible, isothermal, non-rotational, and laminar. The Navier-Stokes and continuity equations for axisymmetric pipe flow take the following form [7]:

$$\rho \left(v \frac{\partial u}{\partial r} + u \frac{\partial u}{\partial x} \right) = -\frac{\partial p}{\partial x} + \mu \left(\frac{\partial^2 u}{\partial r^2} + \frac{1}{r} \frac{\partial u}{\partial r} + \frac{\partial^2 u}{\partial x^2} \right), \quad (1)$$

$$\rho \left(v \frac{\partial v}{\partial r} + u \frac{\partial v}{\partial x} \right) = -\frac{\partial p}{\partial r} + \mu \left(\frac{\partial^2 v}{\partial r^2} + \frac{1}{r} \frac{\partial v}{\partial r} - \frac{v}{r^2} + \frac{\partial^2 v}{\partial x^2} \right), \quad (2)$$

$$\frac{\partial v}{\partial r} + \frac{v}{r} + \frac{\partial u}{\partial x} = 0, \quad (3)$$

where ρ is density, u is velocity along the pipe in the x -direction, v is the radial velocity in the r -direction, μ is the dynamic viscosity, and p is the pressure.

For the special case of fully-developed flow the Navier-Stokes and continuity equations take the following form,

$$\frac{dp}{dx} = \mu \left(\frac{d^2 u}{dr^2} + \frac{1}{r} \frac{du}{dr} \right), \quad (4)$$

$$\frac{du}{dx} = 0. \quad (5)$$

Equation (5) is important for understanding that the velocity through the pipe is only in the x -direction and the velocity profile does not vary once the flow is fully-developed. From here forward, in this thesis, velocity will only be considered in the streamwise direction, u .

The solutions for both entrance and fully-developed regions are presented for the cases of Newtonian, Bingham Plastic, Power Law, and Herschel-Bulkley flows. The solutions to a Newtonian flow are presented in order to validate the solutions from two commercial software solvers, Star-CCM+ and Solidworks Flow Simulation. In each of the flow types, several flow characteristics are calculated through the equations and are compared with the solutions from the computational solvers. These are velocity profiles, pressure differential, wall shear stress, and boundary layer thickness. The equations are presented in the order in which they were used. For all fluid types discussed in the thesis the equations for the fully-developed region are analytical, and those presented for the entrance region are approximate solutions.

Newtonian Flow Solutions

Since the pipe geometry is predetermined, a Reynolds number is chosen in the laminar regime and the average velocity, u_{ave} , is obtained first.

$$Re_d = \frac{\rho u_{ave} D}{\mu} \quad (6)$$

Shah and London [8] present an approximation of the entrance length, L_{fd} , of a pipe of diameter D ,

$$\frac{L_{fd}}{D} = \frac{.6}{1 + .035Re_d} + 0.56Re_d. \quad (7)$$

Equation (7) is used to find the length of the pipe required for a flow to become fully developed . The calculated pipe length is used as a minimum value for the pipe that is modeled in each of the computational domains.

Another important parameter is the velocity profile or velocity as a function of radius in a fully developed pipe range, $u(r)$. This is found from Equation (4), [9]

$$u(r) = \frac{1}{4\mu} \frac{dp}{dx} (R^2 - r^2), \quad (8)$$

where R is the radius of the pipe.

The average velocity is obtained by integrating Equation (8) over the radius of the pipe. The Reynolds number is related to the pressure gradient, dp/dx through the following equation:

$$u_{ave} = \left(-\frac{dp}{dx} \right) \frac{R^2}{8\mu}. \quad (9)$$

Another key parameter is the wall shear stress, τ_w , which is related to the pressure differential through the following equation:

$$\tau_w = -\mu \frac{du}{dr} = -\frac{R}{2} \frac{dp}{dx}. \quad (10)$$

The wall shear stress equation is not unique to laminar Newtonian flow as it is valid for all fluid types and turbulent flows [9],

Within the entrance length of the pipe the velocity profile changes from a constant velocity profile at the entrance to the parabolic shape as is described by Equation (8). This acceleration of fluid is a result of the wall friction and mass conservation. [10] Works by B. Punnis [11] describes a method to approximate the velocity of fluid within this region. The solution to this problem requires only the average velocity of the fluid and the position along the pipe. The output gives the velocity over the radius of the pipe, $u(r)|_{x=x_i}$, where x_i is the position along the axis of the pipe.

$$u(r)|_{x=x_i} = 2u_{ave}(\psi'_1 + \psi'_2 C_1 e^{-2\lambda_1 \epsilon^2}) \quad (11)$$

where,

$$\epsilon = \sqrt{\frac{\mu x}{\rho R^2 u_{ave}}}. \quad (12)$$

The constants C_1 and λ_1 are derived specifically for laminar Newtonian flow in pipes:

$$C_1 = 2.421 \quad \lambda_1 = 8.0196,$$

The other two constants ψ'_1 and ψ'_2 are specific to locations along the radial distance from the center as shown in Table 1.

Table 1: Numerical entrance velocity constants [11]

r/R	ψ_1'	ψ_2'
0	1	-0.1589
0.02	0.9996	-0.1585
0.04	0.9984	-0.1573
0.06	0.9964	-0.1554
0.08	0.9936	-0.1526
0.1	0.99	-0.1491
0.12	0.9856	-0.145
0.14	0.9804	-0.1401
0.16	0.9744	-0.1346
0.18	0.9676	-0.1286
0.2	0.96	-0.122
0.22	0.9516	-0.115
0.24	0.9424	-0.1076
0.26	0.9324	-0.0991
0.28	0.9216	-0.0919
0.3	0.91	-0.0837
0.32	0.8976	-0.0754
0.34	0.8844	-0.067
0.36	0.8704	-0.0586
0.38	0.8556	-0.0503
0.4	0.84	-0.0422
0.42	0.8236	-0.0342
0.44	0.8064	-0.0265
0.46	0.7884	-0.0191
0.48	0.7696	-0.0121
0.5	0.75	-0.0054
0.52	0.7296	0.0008
0.54	0.7084	0.0066
0.56	0.6864	0.0119
0.58	0.6636	0.0167
0.6	0.64	0.021
0.62	0.6156	0.0247
0.64	0.5904	0.0279
0.66	0.5644	0.0305
0.68	0.5376	0.0326
0.7	0.51	0.0341
0.72	0.4816	0.0331
0.74	0.4524	0.0335

0.76	0.4224	0.0355
0.78	0.3916	0.0345
0.8	0.36	0.0338
0.82	0.3276	0.0323
0.84	0.2944	0.0303
0.86	0.2604	0.0279
0.88	0.2256	0.0251
0.9	0.19	0.0218
0.92	0.1536	0.0182
0.94	0.1164	0.0141
0.96	0.0784	0.0098
0.98	0.0396	0.0051
1	0	0

The centerline velocity is found from evaluating Equation (11) at the center of the pipe where $r = 0$. The entries found on the first line of Table 1 correspond with this location and the approximation for the centerline velocity in the entrance region of the pipe becomes,

$$\begin{aligned}
 u_c(x) &= 2u_{ave} \left(1 + (-0.1589)(2.421)e^{-2(8.0196)\epsilon^2} \right) \\
 &= 2u_{ave} \left(1 - .38469e^{-16.0392\epsilon^2} \right).
 \end{aligned} \tag{13}$$

Equation (13) is used to plot the Punnis approximation of the centerline velocity with the centerline velocities found from the simulations. This is provided to compare the closeness of the simulated results to the results found from the Punnis approximation.

Once the centerline velocities are found for the locations of interest along the entrance length of the pipe, the boundary layer thickness for each location can be found. The Blasius solution with and without a pressure gradient is used in the current study to find the boundary layer thickness at each location. The Blasius to include a pressure gradient was derived by Falkner and Skan [12],

$$\eta = y \sqrt{\frac{m+1}{2} \frac{u_c(x)}{\nu x}}, \tag{14}$$

and is a close approximation to the boundary layer thickness either with a pressure gradient or without. Both approaches are discussed in this thesis. In Equation (14), y is the distance from the wall and has the value $y = R - r$, ν is the kinematic viscosity, and η corresponds to a non-dimensional velocity value $f'(\eta) = u/u_c(x)$ (see Table 2).

Table 2: Tabulated Blasius solution for laminar flow over a flat plate [9]

η	$f(\eta)$	$f'(\eta)$
0	0	0
0.1	0.0024	0.047
0.2	0.0094	0.0939
0.3	0.0211	0.1408
0.4	0.0376	0.1876
0.5	0.0586	0.2342
0.6	0.0844	0.2806
0.7	0.1147	0.3265
0.8	0.1497	0.372
0.9	0.1891	0.4167
1	0.233	0.4606
1.2	0.3337	0.5453
1.4	0.4507	0.6244
1.6	0.583	0.6967
1.8	0.7289	0.7611
2	0.8868	0.8167
2.2	1.055	0.8633
2.4	1.2315	0.9011
2.6	1.4148	0.9306
2.8	1.6033	0.9529
3	1.7956	0.9691
3.2	1.9906	0.9804
3.4	2.1875	0.988
3.5	2.2863	0.9907
4	2.7839	0.9978
4.5	3.2832	0.9994

Both Schetz and Punnis make reference to the changing centerline velocity and present a non-linear dependence on centerline location given by,

$$u_c(x) = u_{ave}x^m. \quad (15)$$

For Punnis, this representation was the precursor to his solution previously mentioned as Equation (13). For Schetz, this applies only to certain wedge flows which evolves into the Blasius solution in which a pressure gradient exists. For these Falkner-Skan wedges the Blasius solution is exact.

It makes sense to use the Blasius solution with a pressure gradient since a pressure gradient exists in the problem. However, Falkner and Skan [12] applied the pressure gradient solution to flow over an inclined flat plate rather than through a horizontal pipe. The dimensionless value, m , is related to the angle of incidence (β) of the flat plate [12]:

$$\beta = \frac{2m}{m + 1}. \quad (16)$$

For the case of the flat plate with zero incidence, $\beta = m = 0$ [12]. In the thesis, for pipe flow, m is obtained from simulated centerline velocities by a curve fit in the form of Equation (15). An interesting correlation between the simulated centerline velocities and the Blasius solution is discussed in the Results section.

Bingham Plastic Flow Solutions

As described in the introduction, the Bingham Plastic model is a Newtonian flow in which the y -intercept is not located at the origin. In other words, the first major departure from the behavior of Newtonian fluids is they require a finite stress to initiate flow, [13]

$$\tau - \tau_o = \mu_p \frac{du}{dr}. \quad (17)$$

τ_o is the stress required to initiate flow, τ is the shear stress, and μ_p is the plastic viscosity, which as Darley [13] wrote is the shear stress in excess of the yield stress that induces a unit rate of shear.

Equation (17) is obtained from the Newtonian stress/strain rate relation [13],

$$\tau = \mu \frac{du}{dr}. \quad (18)$$

Let $\gamma = du/dr$. The viscosity is not independent of shear rate. By convention, the expression used to designate the viscosity of non-Newtonian fluids is,

$$\mu_e = \frac{\tau}{\gamma}, \quad (19)$$

where μ_e is the ‘effective’ viscosity. This is used to emphasize that the shear rate at which the viscosity is measured needs to be stipulated [1]. The initial yield stress term from Equation (17) is moved to the right side and the substitution for γ is used,

$$\tau = \mu_p \gamma + \tau_o, \quad (20)$$

where μ_p is the plastic viscosity. The substitution is made from Equation (19) to get the result for the effective viscosity,

$$\mu_e = \mu_p + \frac{\tau_o}{\gamma}. \quad (21)$$

For purely Bingham Plastic fluids the flow would initiate once the initial shear stress value had been met. Thus a required initial pressure, P_o , is found from τ_o and the length of the pipe, L , [13]

$$\tau_o = \frac{R P_o}{2 L}. \quad (22)$$

If pressure is slowly increased from atmospheric pressure, the flow of a Bingham Plastic would begin as a uniform motion where the velocity gradient was a straight vertical line across the axis of the pipe, according to Darley [13]. Laminar flow would not begin until the initial shear stress was met at a critical pressure. At greater pressures than P_o laminar flow would progress toward the axis of the pipe. This implies that there is always fluid with a critical radius (called the plug radius) that moves over this laminar flow and is related to the pressure. Hanks [14] describes the non-linear relation that the pressure has on flow rate. Analysis shows this relation becomes linear and the asymptote always crosses at $\frac{4}{3}P_o$ as shown in the figure below,

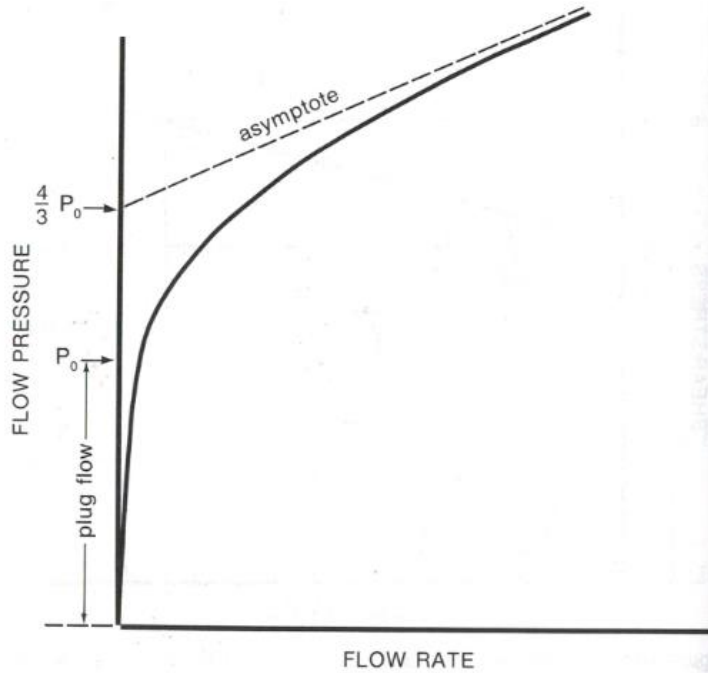


Figure 3: Pressure vs. flow rate Darley [13]

$$Q = \frac{\pi R^4}{8\mu_p L} \left[P - \frac{4}{3} P_0 \left(1 - \frac{P_0^3}{4P^3} \right) \right]. \quad (23)$$

Equation (23) is the approximated flow rate for Bingham Plastic flow from Darley [13]. This is useful with fairly good accuracy for flows under much higher pressures than P_0 . The Buckingham-Reiner equation is more useful for creeping flows where the plug radius is of consequence. Steffe [15] points out that the flow profile is discontinuous and must be integrated over each region to obtain the exact flow rate,

$$Q = \frac{\pi R^4 \delta P}{8\mu_p L} \left[1 - \left(\frac{4}{3} \right) \left(\frac{\tau_0}{\tau_w} \right) + \left(\frac{1}{3} \right) \left(\frac{\tau_0}{\tau_w} \right)^4 \right]. \quad (24)$$

The correlation of the stress terms to the pipe radius and the critical plug radius

$c = \frac{R_c}{R} = \frac{\tau_o}{\tau_w}$ is substituted into Equation (24),

$$Q = \frac{\pi R^4 \delta P}{8\mu_p L} \left[1 - \left(\frac{4}{3}\right) \left(\frac{R_c}{R}\right) + \left(\frac{1}{3}\right) \left(\frac{R_c}{R}\right)^4 \right]. \quad (25)$$

The differential pressure, δP , refers to the total change in pressure over the length of the pipe and is described by $\delta P = P - P_o$. Steffe [15] goes further to derive the fully developed velocity profile, $u(r)$,

$$u(r) = \frac{\delta P R^2}{4\mu_p L} \left[1 - \left(\frac{r}{R}\right)^2 - \frac{2R_c}{R} \left(1 - \frac{r}{R}\right) \right]. \quad (26)$$

The critical plug radius (R_c) and plug velocity (u_p) can be defined as [15],

$$R_c = \frac{\tau_o 2L}{\delta P}, \quad (27)$$

$$u_p = \frac{\delta P R^2}{4\mu_p L} \left[\left(1 - \frac{R_c}{R}\right)^2 \right]. \quad (28)$$

The exact relation of the stress terms in the Bingham Plastic fluid model compared to the Newtonian fluid model implies validity for the Blasius approximation approach to pipe flow. As Schetz [9] found the shear stress term appears in the momentum equation as $\partial\tau/\partial y$ then the Blasius solution applies equally to Bingham Plastic fluids as it does for Newtonian fluids.

Power Law Flow Solutions

Since Equation (18) works for all fluid types then we start by looking at this relation and how it could relate to a fluid whose viscosity changes as a function of shear rate. If this were a purely Newtonian fluid then the shear stress to rate of strain relation is 1, but with shear thinning fluids this relation is described as a power index of a value less than 1. Shear thickening index values are greater than 1. Equation (18) is modified to include the power index,

$$\tau = \mu_{pl} \left(\frac{du}{dr} \right)^p, \quad (29)$$

where p is the index value. [9] The expression is solved by integrating over r and from Schetz [9] the fully-developed velocity profile along the radius becomes,

$$u(r) = \left(\frac{\tau_w}{\mu_{pl}} \right)^{\frac{1}{p}} \frac{R}{\left(\frac{1}{p} \right) + 1} \left[1 - \left(\frac{r}{R} \right)^{1 + \left(\frac{1}{p} \right)} \right]. \quad (30)$$

Steffe [15] derives the flow rate for power law fluids in which the differential pressure is known,

$$Q = \pi \left(\frac{\delta P}{2L\mu_{pl}} \right)^{\frac{1}{n}} \left(\frac{n}{3n + 1} \right) R^{\frac{3n+1}{n}}. \quad (31)$$

Since the flow rate is known this equation is useful for determining the differential pressure. This is accomplished by setting $\frac{dp}{dx} = \frac{\delta P}{L}$ and μ_{pl} is the consistency coefficient or plastic viscosity found from the specific fluid data. This is covered later in the next section.

The Reynold's number as it relates to the pipe diameter ($Re_{pl,D}$) is also found from Schetz [9].

$$Re_{pl,D} = \frac{\rho u_{ave}^{2-p} D^p}{\mu_{pl}} 8 \left(\frac{p}{6p+2} \right)^p. \quad (32)$$

Notice that for $p = 1$ the Newtonian relation is recovered.

It follows that there should be some analogy for the Blasius solution concerning power law fluids. The following relation is presented by Acrivos et al, [16]

$$\eta_{pl} = y \left(\frac{\rho u_c^{2-p}}{\mu_{pl} x} \right)^{\frac{1}{p+1}}. \quad (33)$$

Equation (33) can be solved for y as for the Newtonian and Bingham Plastic case and Table 2 is used for the entry, η , in order to get the velocity profiles at each position, x .

Herschel-Bulkley Flow Solutions

Cheremisinoff [17] wrote, "The Herschel-Bulkley model may be thought of as a hybrid between the Power Law and Bingham Plastic models and is essentially the Power Law model with a yield stress." This assertion is represented in Equation (34) in which the yield stress, τ_o , is added,

$$\tau = \mu_{pl} \left(\frac{du}{dr} \right)^p + \tau_o. \quad (34)$$

Equations (10) and (27) are still valid to find the wall shear stress and plug radius. Steffe [15] uses the same methods as in the Power Law and Bingham Plastic models to derive the fully developed velocity profile,

$$u(r) = \frac{2L}{\delta P \left(1 + \left(\frac{1}{p}\right)\right) \mu_{pl}^{\frac{1}{p}}} \left[(\tau_w - \tau_o)^{1 + \left(\frac{1}{p}\right)} - \left(\frac{\delta P r}{2L} - \tau_o\right)^{1 + \left(\frac{1}{p}\right)} \right]. \quad (35)$$

The plug velocity is found by setting $r = R_c$ in Equation (35) once the plug radius is found.

The entrance velocity is obtained from a separate source and works in agreement with the work done by Steffe. El-Nahhas [18] describes the entrance velocity, u_e , first and the flow rate is obtained from the relation to the cross-sectional area, A , where $Q = Au_e$.

$$u_e = \frac{nR}{\tau_w^3 \mu_{pl}^{\frac{1}{p}}} (\tau_w - \tau_o)^{\frac{p+1}{p}} \left[\frac{(\tau_w - \tau_o)^2}{1 + 3p} + \frac{2\tau_o(\tau_w - \tau_o)}{1 + 2p} + \frac{\tau_o^2}{1 + p} \right]. \quad (36)$$

In the thesis, the boundary layer thickness and velocity profiles in the entrance region of the pipe are found using the same Blasius approximation used in the Bingham Plastic and Newtonian cases.

DRILLING FLUID RHEOLOGY

Drilling fluids, often referred to as Muds, are characterized by viscosity, plastic viscosity (PV), and yield point (YP) that is measured by a device that spins a sleeve inside a sample cup at specified rates. Inside the sleeve is a stationary spring loaded weight which reacts to the viscous forces in the fluid. The device, called a Fann meter, displays the angular difference of the spring loaded weight from its resting position. This angular difference changes as the rate of rotation changes, and this information is used in a fluid model to obtain the stress-to-strain rate relation.

The drilling fluid used in this thesis is unique and the data collected by the author pertains to this drilling fluid only. The drilling fluid properties were measured for this study using a Fann meter and are presented in Table 3. The units used are typical in the drilling industry. The mud weight is measured in pounds per gallon (ppg) and the dynamic viscosity and plastic viscosity (PV) is measured in centipoise (cP). The yield point (YP) is a stress measurement in pounds per 100 square feet. The angular velocity is measured in revolutions per minute (rpm) The apparent viscosity (AV) is synonymous with the effective viscosity, μ_e .

Table 3: Measured drilling fluid rheology

Fann Speed	Fann Reading
600 rpm	51
300 rpm	29
200 rpm	21
100 rpm	14
6 rpm	5
3 rpm	4
PV	22 cP
YP	7 lbs/100sq.ft.

The data from Table 3 are shown by circles in Figure 4. This data is used to find a curve fit corresponding to various fluid models considered in this thesis by methods outlined in the Drilling Fluids Processing Handbook. [1] The equations produced are an intermediate step to finding the coefficients that are used in the simulations and analysis. Once the curve fit equation is found for a particular fluid model the units are converted to a format that can be input into the simulation software or used to obtain an analytical solution.

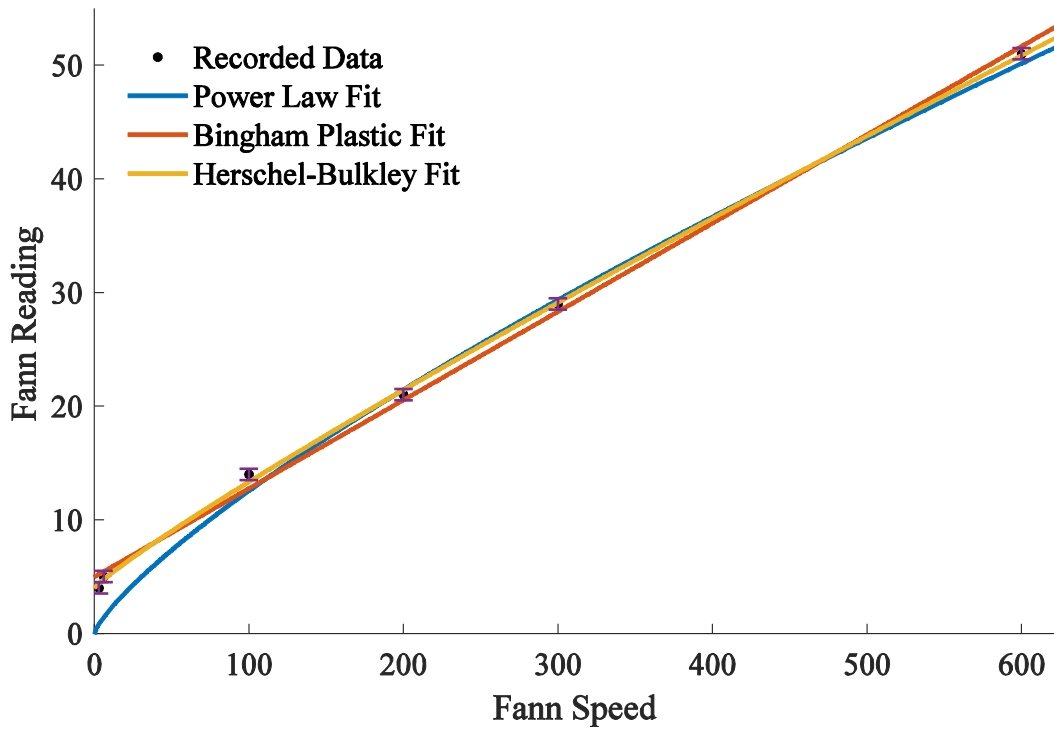


Figure 4:Fann data and curve fit for Bingham Plastic, Power Law, and Herschel-Bulkley models

The Power Law curve fit equation is presented as Equation (37)

$$Fann Reading = .3579(Fann Speed)^{.7727} \quad (37)$$

The units in the curve fit equation are in terms of *rpm* and have a ratio to *rad/s* of 1:1.7. This is used to rearrange Equation (37) to a form that can be used in the simulation software and the analysis,

$$\tau = 0.1137\omega^{0.7727}. \quad (38)$$

This form is consistent with the Power Law model for stress in Equation (29) where τ has units of pascals (*Pa*), and the coefficient, $\mu_{pl} = 0.1137$, has units of pascal seconds (*Pa · s*).

The curve fit obtained using the Bingham Plastic model applies to the experimental data in Figure 4 and is shown by the red curve the following equation,

$$Fann\ Reading = 0.07782(Fann\ Speed) + 4.986. \quad (39)$$

The Bingham Plastic model is linear like the Newtonian model but with the y-intercept not at zero. The process of converting the curve fit equation to the one used in the simulations and analysis is the same as in the Power Law model case, which gives:

$$\tau = 0.0219\omega + 2.387. \quad (40)$$

The Power Law curve fit underestimates the low rate shear stress while the Bingham Plastic curve fit overestimates the low rate shear stress [1]. This can be seen from Figure 4 where the Power Law curve fit (shown in blue) is seen not to capture the Fann data points at 3 and 6 *rpm*. For this reason the Herschel-Bulkley model is preferred since it provides a more accurate fit over the entire range of values. The curve fit to the data using the Herschel-Bulkley model is shown in Figure 4 by the red color and is given by the following equation:

$$Fann\ Reading = 0.1474(Fann\ Speed)^{.9007} + 4.021. \quad (41)$$

Equation (41) in the form similar to Equation (34) is:

$$\tau = 0.0438\omega^{0.9007} + 1.925. \quad (42)$$

Whichever drilling fluid model is used helps to determine the operating parameters for the pumps and motors at the drilling site. In the drilling industry, it is important to have a fluid that exhibits low apparent viscosity at high shear rates. This feature reduces the amount of power required to drive the fluid through the bit. It is also important for the fluid to have high apparent viscosity in the annulus of the drilled hole where the shear rate is greatly reduced. The reason for this is to carry the cuttings to the surface. Nearly all drilling fluids are shear-thinning for these reasons. Thus, the fluid model used must capture the Fann data within reasonable accuracy.

Both Power Law and Bingham Plastic fluid models are useful at high shear rates, but the differences between the two models are apparent at low shear rates. This is shown through the calculation of the effective viscosity using Equation (43), [1]

$$\mu_e = \frac{Fann\ Reading \times 511}{Fann\ Speed \times 1.7}. \quad (43)$$

The units in equation (43) are given in centipoise, cP. For the Power Law model, the effective viscosity at 3 rpm was 84 cP. compared to 522 cP at 3 rpm in the Bingham Plastic case. The difference between these two values is drastic and could predict very wrong values for flow rate required for cutting removal and thus power required. A closer fit to the Fann values would give a more realistic value for the viscosity at low shear rates. The Herschel-Bulkley model does this.

The coefficients for the fluid models found from the experiment and used in the thesis are compiled (see Table 4).

Table 4: Model coefficients

ρ	1198.4 kg/m^3
μ_p (Bingham Plastic)	0.0219 $Pa \cdot s$
τ_o (Bingham Plastic)	2.387 Pa
μ_{pl} (Power Law)	0.1137 $Pa \cdot s$
p (Power Law)	0.7727
μ_{pl} (Herschel-Bulkley)	0.0438 $Pa \cdot s$
n (Herschel-Bulkley)	.9007
τ_o (Herschel-Bulkley)	1.925 Pa

NUMERICAL PROCEDURE

The analytical results, obtained from Equations (6)-(16), from the fully-developed Newtonian fluid flow are used to validate the simulation results obtained from two commercial software platforms, Star-CCM+ [6] and SolidWorks Flow Simulation [5]. Two sets of input parameters are used in Star-CCM+ which corresponds to a course mesh and a fine mesh. Convergence of residuals from the simulations conducted using the two meshes are used to determine which mesh will be used in the cases with non-Newtonian flow. It is also used for validation against the analytical solution and Solidworks Flow Simulation results for Newtonian flow. Solidworks Flow Simulation is used for the flow simulations of the Bingham Plastic, Power Law, and Herschel-Bulkley models of the drilling fluid using the course mesh.

Computational Domain and Boundary Conditions

The pipe dimensions used in the simulations have a length of $1.5m$ and a diameter of $0.02m$. This volume is discretized with a greater concentration of cells closer to the wall. Table 5 and Table 6 provide the grid parameters of the coarse mesh and the fine mesh used in the simulations.

Table 5: Mesh parameters (coarse mesh)

Mesh type: rectangular
Base cell size: .01m
Max cell size relative to base: 10000%
Min cell size relative to base: 5%

Table 6: Mesh parameters (fine mesh)

Mesh type: rectangular
Base cell size: .001m
Max cell size relative to base: 100%
Min cell size relative to base: 23%

The smallest cell closest to the wall in the fine mesh has an edge length of $2.3 \times 10^{-4} m$ or $\frac{1}{43}$ radius and the coarse mesh has a wall cell edge length of $5 \times 10^{-4} m$ or $\frac{1}{20}$ radius. The fine mesh contains 6.5 million cells while the coarse mesh contains 1.2 million cells. The simulation residuals are evaluated in Star-CCM+ and used to find the details of convergence.

At the entrance, the fluid velocity is set to be constant and uniform over the cross-sectional area of the pipe, and the boundary condition at the exit is set to a pressure opening equal to atmospheric pressure.

The inlet fluid velocity is found by stipulating a Reynolds number known to be laminar and finding the associated velocity. Since the Reynolds number decreases with an increase in viscosity the least viscous fluid should be used to find the Reynolds number for the pipe modeled to be within the laminar regime. The density and dynamic viscosity for water at 20°C are used [19]:

$$\rho = 998 \text{ kg/m}^3$$

$$\mu = .001002 \text{ kg/m} \cdot \text{s}$$

The diameter related Reynolds number, Re_d , is specified to be 1,200 as this value falls within the acceptable range for laminar flows [9]. Using Equation (6) the entrance velocity is found and from Equation (9) the differential pressure is found. The entrance length is also found using Equation (7). the flowrate is easily found by multiplying the cross-sectional area of the pipe and the entrance velocity shown here as Equation (44). Some flow parameters for the Newtonian flow are shown in Table 7.

$$Q = \pi R^2 u_{ave} \quad (44)$$

Table 7: Flow parameters for water

u_{ave}	0.0624 m/s
Q	$1.96e - 5 \text{ m}^3/\text{s}$
dp/dx	5.69 Pa/m
L_{fd}	1.39 m

RESULTS

Simulation Convergence for Both Meshes

With the flow parameters set the simulations are run for both meshes in Star-CCM+. The following two plots in Figure 5 show the grid convergence results for each mesh. The residual plot shows the difference between solutions obtained at consecutive iterations. The y and z -directions, when described in the cylindrical coordinate system for an axisymmetric flow, are represented by the single axis, r .

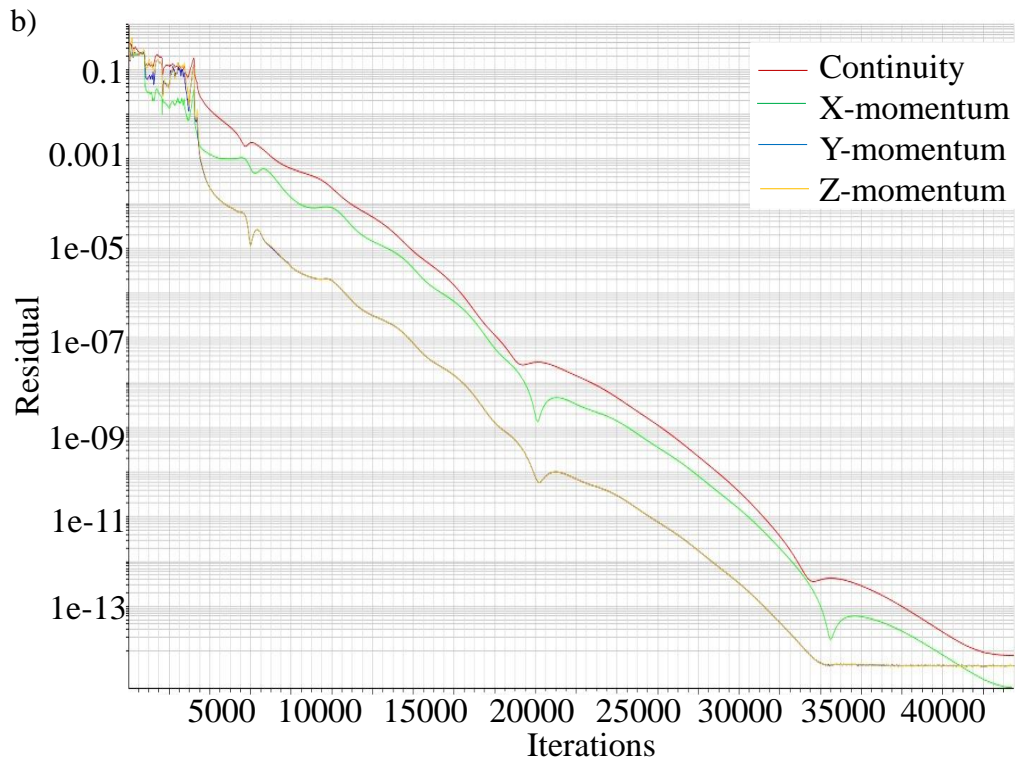
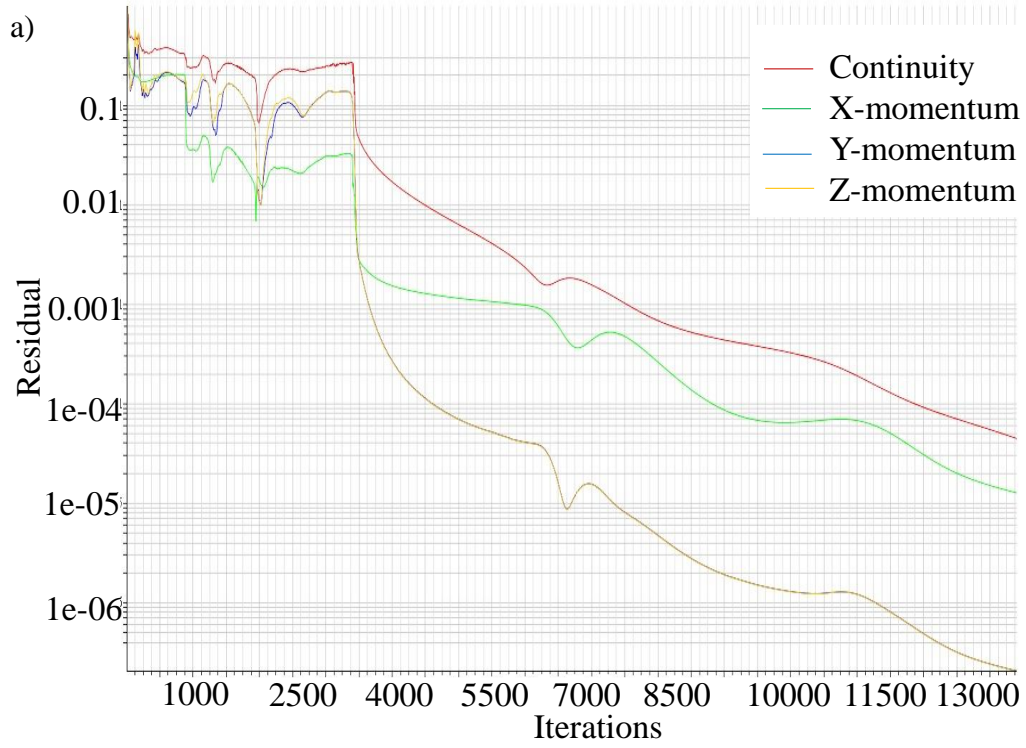


Figure 5: Residual plots for simulations run in Star-CCM+; a) Fine mesh, b) Coarse mesh

All coarse mesh residuals in Figure 5 converge at about 42,600 iterations. The residual values are lower than 10^{-14} when the simulation is terminated.

The fine mesh simulation is terminated at 13,339 iterations due to the unchanging velocity profile and the closeness between the coarse and fine mesh velocity profiles. This is shown in Figure 6. While the continuity residual value in the fine mesh simulation reaches 10^{-5} by the end of the simulation, the velocity profiles are nearly matched between the coarse mesh and the fine mesh (refer to Figure 6). In the figure, the solid lines are the fine mesh results and the dashed lines are the coarse mesh results. The non-dimensional axis labels are defined as $u^+ = U/u^*$ where U is the fluid velocity at a radius, r , and $u^* = u_c \sqrt{\frac{\tau_w}{\rho u_c^2}}$. Also, $y^+ = yu^*/\nu$. As previously mentioned, y denotes the distance from the pipe wall.

The velocity profiles obtained from the fine and coarse meshes are very similar with the simulation on the coarse grid being computationally less expensive. The fine mesh simulation requires 181.1 hours to run 13,339 iterations or almost 49 sec/iteration. The coarse mesh simulation requires 137.9 hours to run 43,287 iterations or 11.7 sec/iteration. The coarse mesh has been chosen for all simulations over the fine mesh since there is no clear advantage of using the finer mesh.

Star-CCM+ Validation using the Analytical Solution of Newtonian Flow

The simulated results from the coarse mesh grid in Star-CCM+ are compared with the analytical solution in terms of the fully developed velocity profile, differential pressure, and wall

shear stress. These analytical parameters are found from Equations (8), (9), and (10), respectively. The results from the analytical calculation and simulation in the fully-developed region conducted with Star-CCM+ are tabulated for water in Table 8.

Table 8: Newtonian (water) results

Analytical	Simulated
$u(0) = 0.0624 \text{ m/s}$	$u(0) = 0.06238 \text{ m/s}$
$u_{fd} = 0.1248 \text{ m/s}$	$u_{fd} = 0.1222 \text{ m/s}$
$L_{fd} = 1.3919 \text{ m}$	$L_{fd} = 1.3499 \text{ m}$
$dp/dx = 5 \text{ Pa/m}$	$dp/dx = 5.69 \text{ Pa/m}$
$\tau_w = 0.0250 \text{ Pa}$	$\tau_w = 0.03 \text{ Pa}$

The values from Table 8 indicate that the simulation results are very close to the analytical solution at least in the fully-developed region of the pipe.

Figure 7 depicts the comparison between the analytical velocity profiles (shown as solid lines) and those of the simulation from Star CCM+ (shown as dashed lines) in the entrance and fully-developed regions. The closeness of the simulation and the results from the analytical solution are good for all positions along the pipe length with the exception of some noticeable difference at the fully developed length, where $x = 140R$.

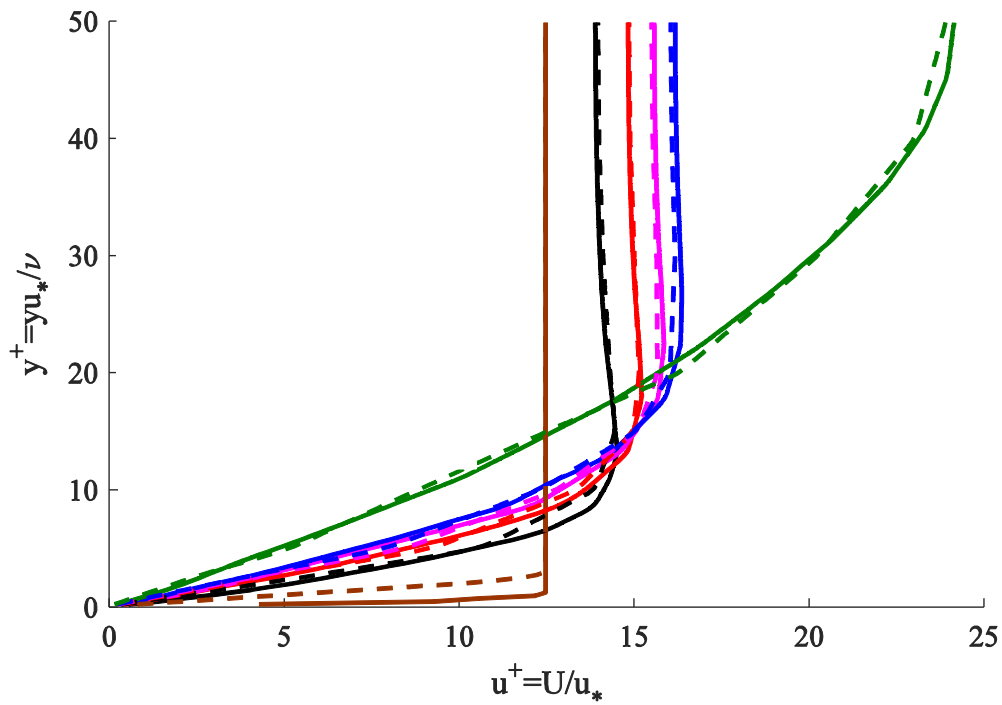


Figure 6: Star-CCM+ water velocity profile mesh comparison, $x = 0R$ (brown), $x = 2R$ (black), $x = 4R$ (red), $x = 6R$ (magenta), $x = 8R$ (blue), $x = 140R$ (green)

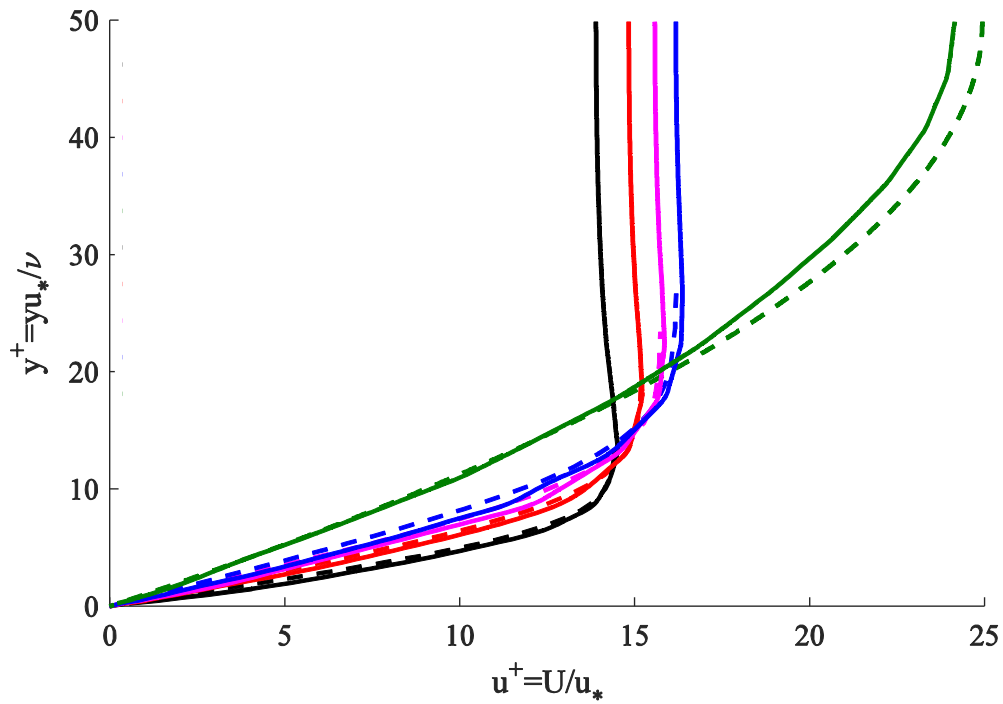


Figure 7: Water velocity profiles for analytical results with a pressure gradient [9] and Star CCM+ results; the color scheme is the same as for Figure 6.

The closeness of the results for the fully-developed section of the pipe obtained from Table 8 and those of the entrance region from Figure 7 validates the simulated results from Star-CCM+.

Figure 8 compares the results obtained from the two software packages. In the figure, the dotted lines are Star-CCM+ fine mesh results, dashed lines are Star-CCM+ coarse mesh results, and the solid lines are the coarse mesh Solidworks Flow Simulation results. As seen from the figure, the results are nearly identical for all positions observed in the pipe. Therefore, in what follows, only the results from Solidworks Flow Simulation are shown.

Extended Pipe Case for Newtonian Flow

In order to ensure that the fully developed velocity had been reached the computational domain is extended to 2.0 *m*. If the fully developed condition met with a pipe length of 1.5 *m* then an extension of the pipe would make no difference to the velocity profile at the location deemed to be fully-developed. The plot in Figure 9 shows the velocity profiles for this extended case along with the velocity profiles obtained from the pipe of the 1.5 *m* length. The solid lines are for the 1.5 *m* pipe and the dashed lines are for the 2.0 *m* pipe. No significant difference between the results obtained in the two pipes are observed, confirming that the fully-developed flow is obtained in the shorter pipe with the length of 1.5 *m*.

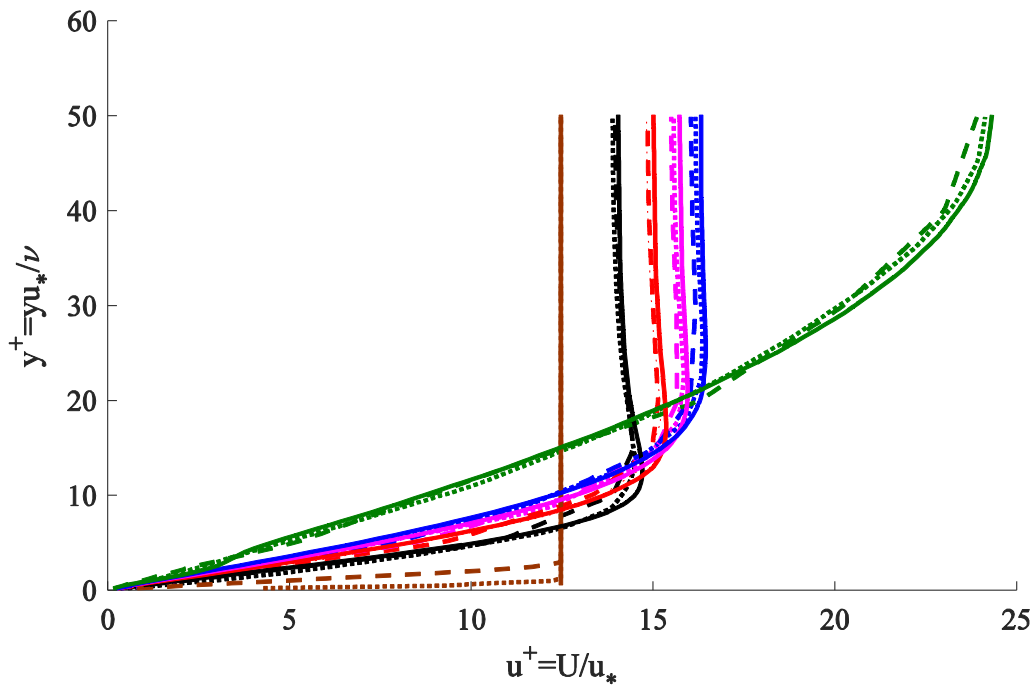


Figure 8: All simulated water velocity profiles; color scheme is the same as in Figure 6

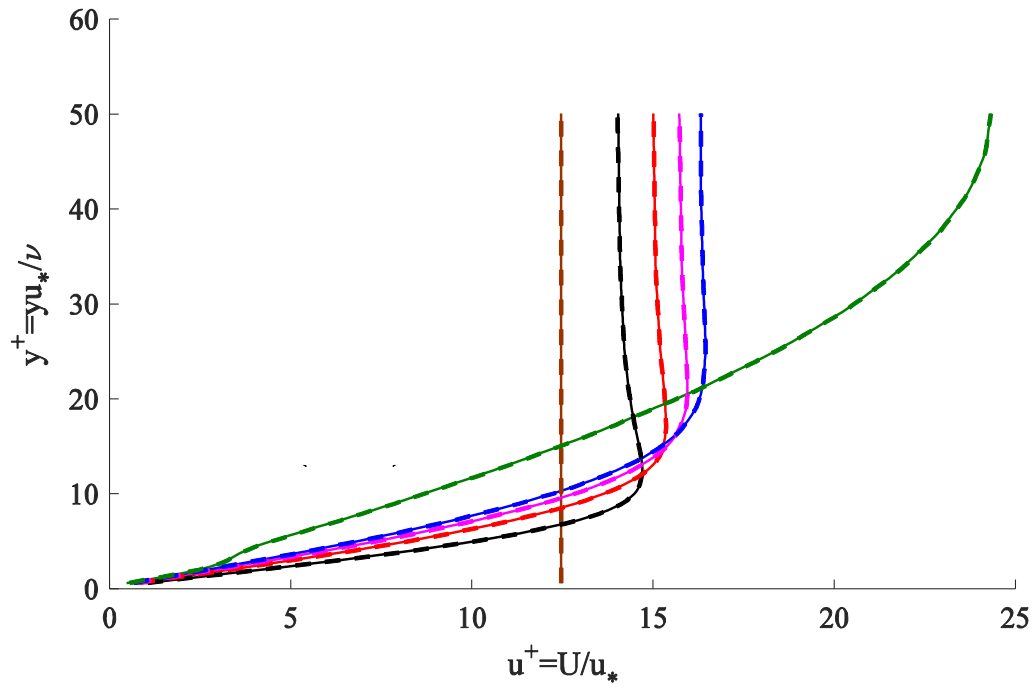


Figure 9: Solidworks coarse mesh simulated velocity profile for water in pipe with a length of 1.5m and 2.0m; color scheme is the same as in Figure 6

Blasius Solution Validation for Newtonian Flow

From Table 8, the value for the pressure gradient is found through the simulation as well as through the analytical solution to Equation (9). Since a pressure gradient exists for the pipe, an attempt is made to use the Blasius solution with a favorable pressure gradient, shown as Equation (14). The entrance region velocity profiles are also found in the case without a pressure gradient in which $m = 0$ in order to compare the closeness of the Blasius solution, with and without a pressure gradient, to the simulated results. For the case with the pressure gradient, the values of the simulated centerline velocities are fitted in the form of Equation (15) which gives the value for m as shown in Figure 10.

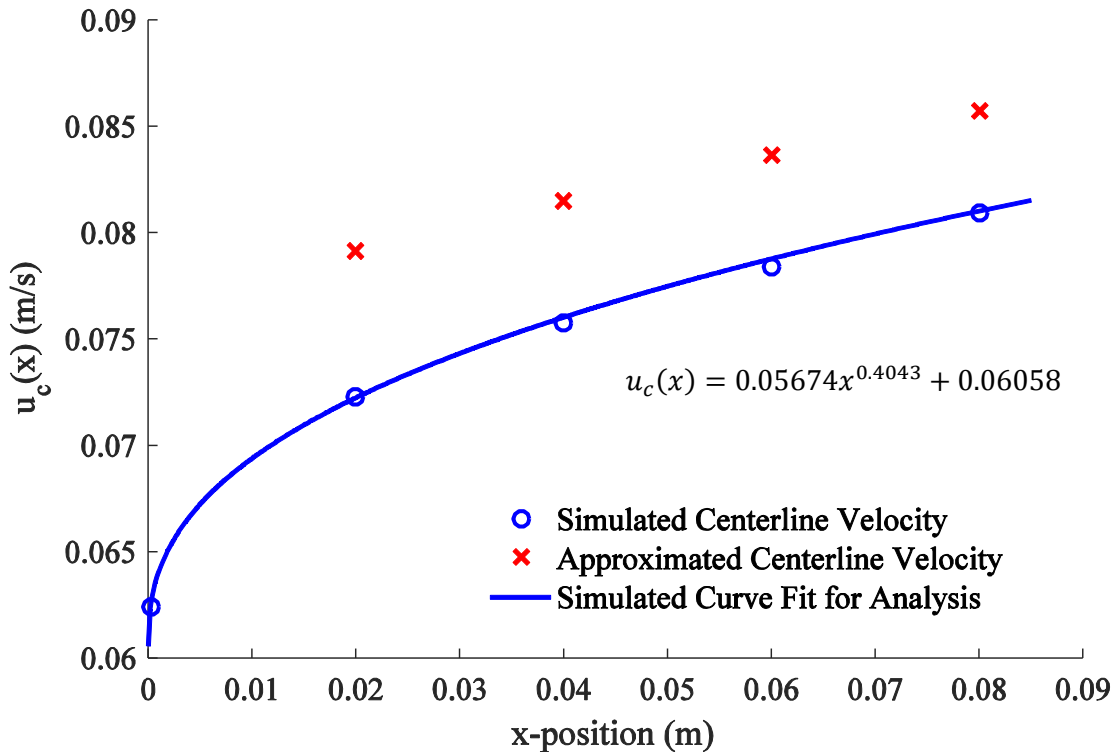


Figure 10: Newtonian simulated centerline velocities with approximated centerline velocities [11]

From Figure 10, the curve fit provides $m = 0.4043$. Equation (14) is used with this value to produce the entrance region velocity profiles. The following figure shows the comparison of the Blasius solution, with and without a pressure gradient, and the simulated results for the Newtonian fluid model entrance region velocity profiles. In Figure 11, y is distance from the pipe wall, δ is the boundary layer thickness, U is the fluid velocity at a distance y , and $U_x = u_c(x)$ evaluated at the position x for that location. In the figure, the symbols are used to denote the analytical solution where red is for the zero pressure gradient calculations and blue is used for the calculation with a pressure gradient. The solid lines indicate simulated results.

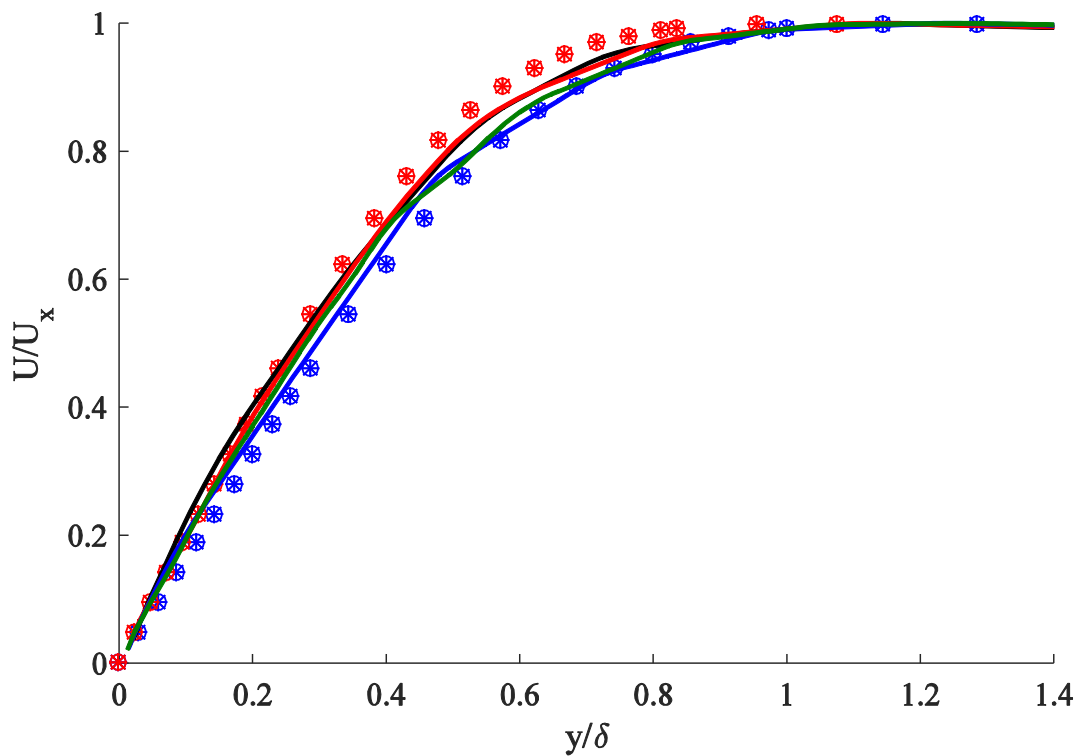


Figure 11: Non-dimensional water velocity profiles for simulated results, zero-pressure gradient, and with pressure gradient analysis [9]; for symbols: $x = 2R$ (o), $x = 4R$ (\times), $x = 6R$ (+), $x = 8R$ (*); for solid lines: $x = 2R$ (black), $x = 4R$ (red), $x = 6R$ (blue), $x = 8R$ (magenta)

The analytical velocity profiles in Figure 11 are self-similar for either case of pressure gradient with or without. It is surprising that the solution remains similar even though the velocity used to generate the curves is changing.

The simulated results from Figure 11 are non-similar and have a range of values which fall in between the analytical results for a pressure gradient and without a pressure gradient. To gain a better understanding of the impact of using the analytical solutions with and without the pressure gradient, the boundary layer thickness is calculated from Equation (14) and the value from Table 2 corresponding to 99% of the centerline velocity. These are compared with the simulated boundary layer thickness and are presented as Figure 12. In the figure, the green line is the simulated boundary layer thickness at each location along x , the red line is the analytical boundary layer thickness with a zero pressure gradient, and the blue line is the analytical boundary layer thickness with a pressure gradient.

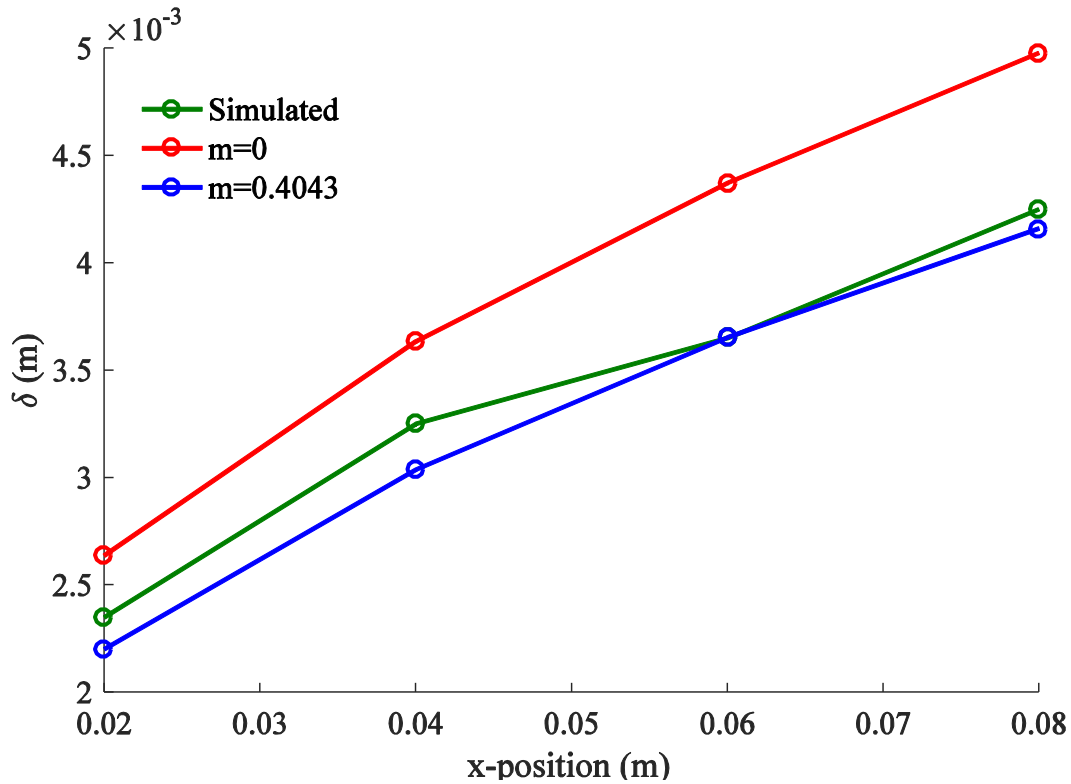


Figure 12: Water boundary layer thickness for simulated results, zero-pressure gradient, and with a pressure gradient [9]

In Figure 12, it is clear that the zero-pressure gradient case of Newtonian flow overestimates the boundary layer thickness. The case of the Newtonian flow with a pressure gradient comes much closer to the simulated results. It is for this reason that the Blasius solution with a pressure gradient is used for the analysis of the non-Newtonian flows. For these analytical solutions the value of m must be found from a curve fit for the simulated centerline velocities for each fluid model.

As a matter of interest, the solution derived by Punnis [11] to find the centerline velocities in the entrance region of a pipe are shown with the simulated results in Figure 10 as a red \times for each location along the pipe. The analytical values for the centerline velocity are found

by Equation (13) and, for the Newtonian results, are consistently higher than the simulated values.

Non-Newtonian Fluid Model Results

A flowrate and inlet velocity is required for the analysis and simulation of the non-Newtonian fluid models. This is accomplished by using Equation (24) in conjunction with the coefficients for the drilling fluid modeled as a Bingham Plastic (see Table 4). A range of pressure is plotted against flowrate using Equation (24) and is presented as Figure 13. A flow rate is then chosen to be $Q = 9 \times 10^{-5} \text{ m}^3/\text{s}$ as a first guess. The corresponding pressure shown in Figure 13 is used to find the differential pressure by Equation (45),

$$\frac{dp}{dx} = \frac{3695 \text{ Pa}}{1.5 \text{ m}} = 2462 \text{ Pa/m.} \quad (45)$$

With the differential pressure known from Equation (45), the critical plug radius is found by inserting the differential pressure value into Equation (27). Figure 14 is produced by Equation (27) to show the sensitivity of the plug radius as a function of the differential pressure. The associated plug radius, $R_c = 0.00207 \text{ m}$, is found from the differential pressure.

The entrance velocity is found using Equation (44). As a check to the flowrate initially stated, the Reynolds number is found from the entrance velocity. Using Equation (6) the Reynolds number is found to be $Re_D \sim 300$ for the Bingham Plastic fluid model. This value changes slightly for the other non-Newtonian fluid models. However, since the Reynolds number is well within the range for laminar flow then the flow rate used as a first guess is suitable for the

rest of the analysis and simulations for all of the non-Newtonian fluid models presented in the thesis [9].

The fully-developed plug velocity and wall shear stress are found using Equations (28) and (10), respectively. Figure 15 shows the analytically derived fully-developed velocity profile of the Bingham Plastic fluid model.

The vertical portion of the velocity profile shown in Figure 15 is the plug diameter. The plug can be viewed as a body of solid material being transported over laminar flow between it and the pipe wall.

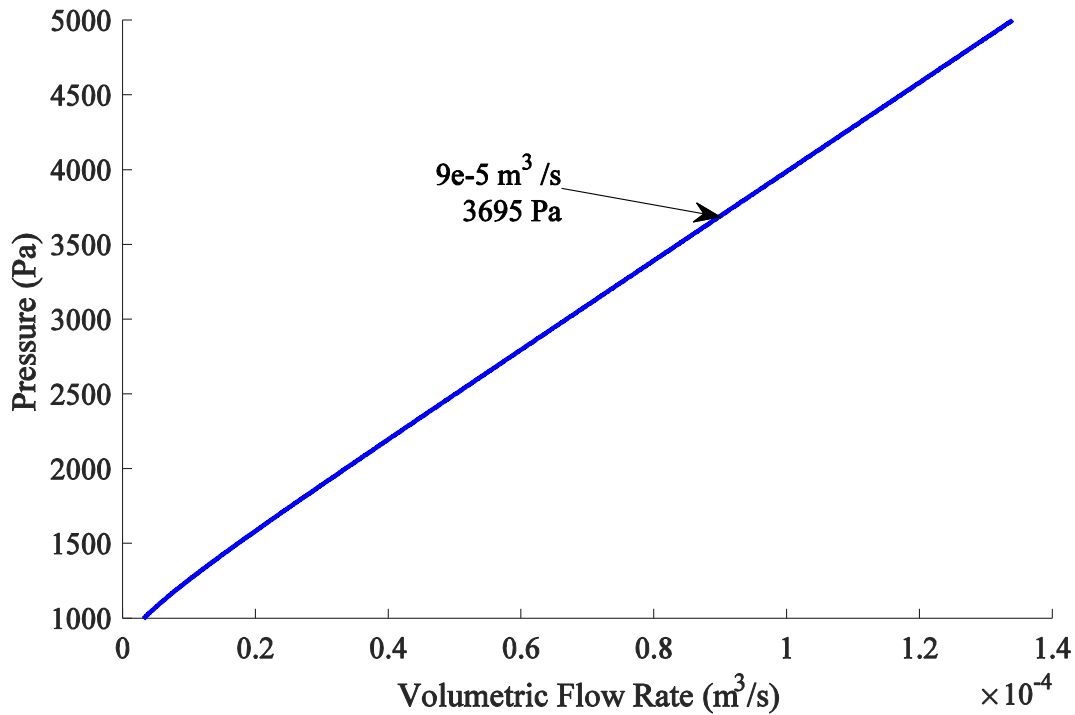


Figure 13: Absolute pressure vs volume flow rate for a Bingham Plastic fluid model [15]

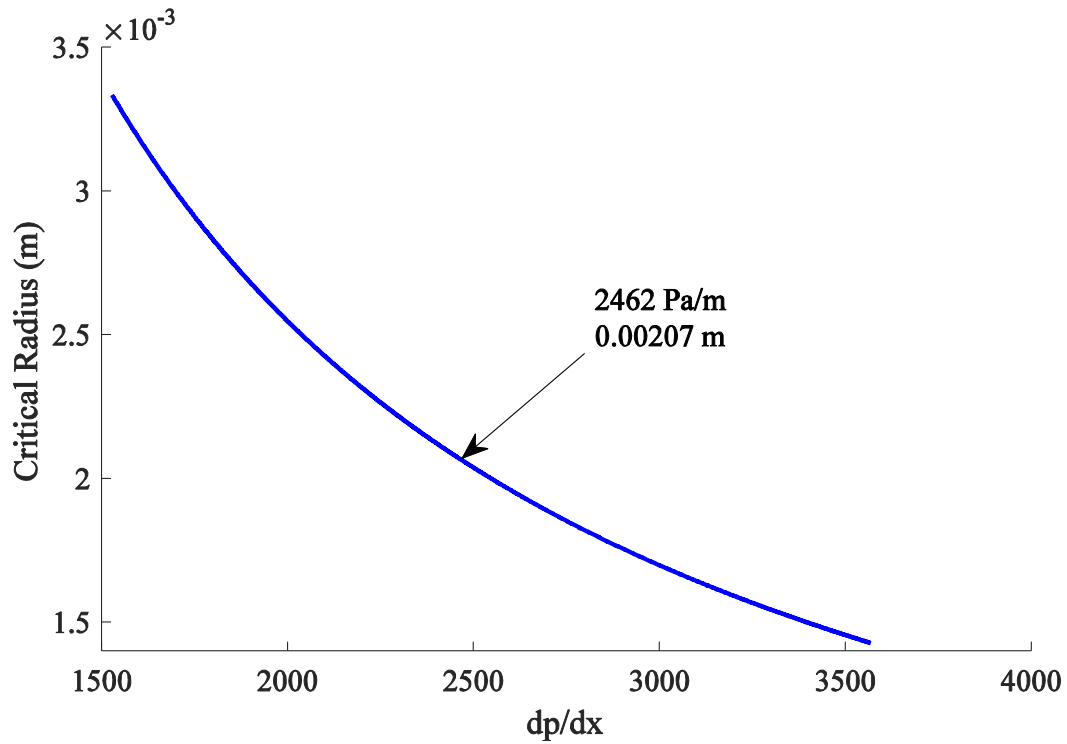


Figure 14: Critical radius vs differential pressure for a Bingham Plastic fluid [15]

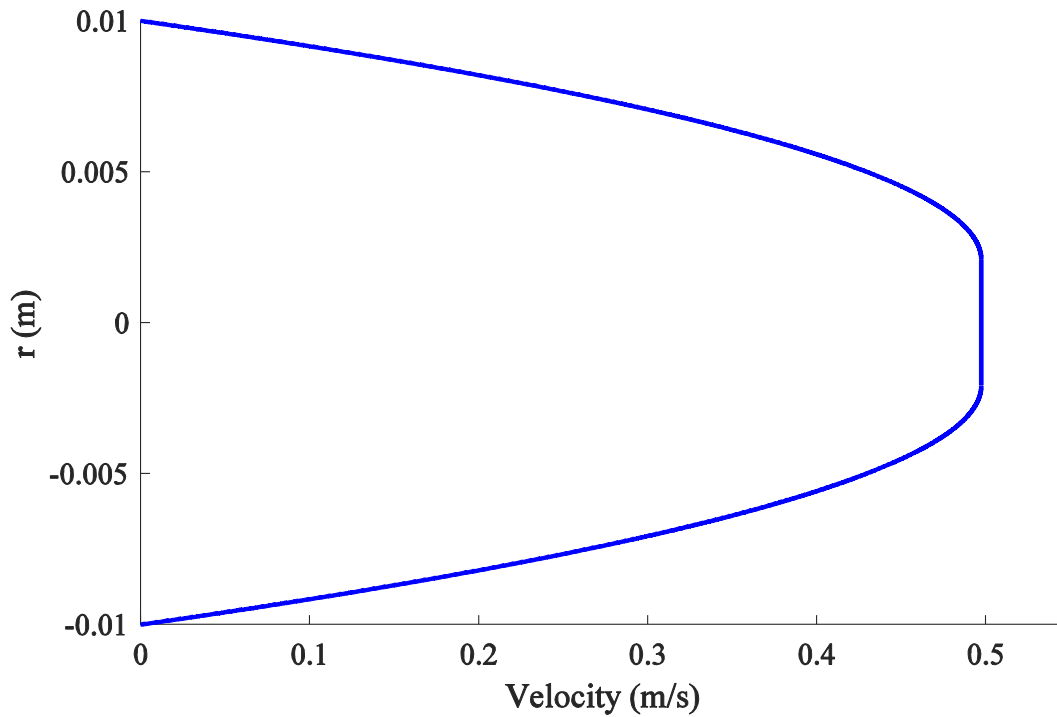


Figure 15: Analytical result for the fully-developed Bingham Plastic velocity profile [15]

In Figures 16-20 the simulated and analytical velocity profiles for each of the fluid models are shown for each location along the axis of the pipe. In the case of the Bingham Plastic fluid model the analytical results are obtained using Equations (26) and (14). For the Power Law fluid model, Equations (33) and (30) are used. In the case of the Herschel-Bulkley fluid model the velocity profiles are found by Equations (14) and (35). It is noteworthy that Acrivos' et al. [16] presentation of the similar solution of the velocity profiles does not include a pressure gradient.

In the figures, the simulated results are represented by solid lines and the analytical results are represented by dashed lines. The colors used are black for Power Law results, red for Bingham Plastic results, and blue for Herschel-Bulkley results.

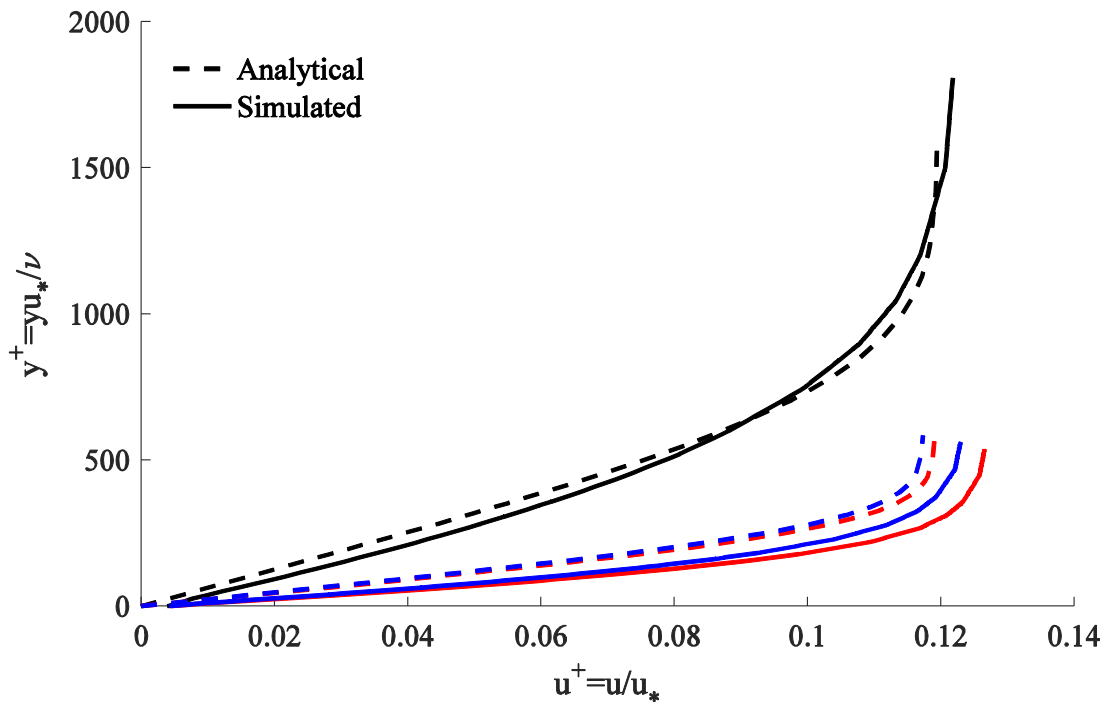


Figure 16: $x = 2R$ analytical and simulated velocity profiles for Power Law [16], Bingham Plastic [9], and Herschel-Bulkley fluid models

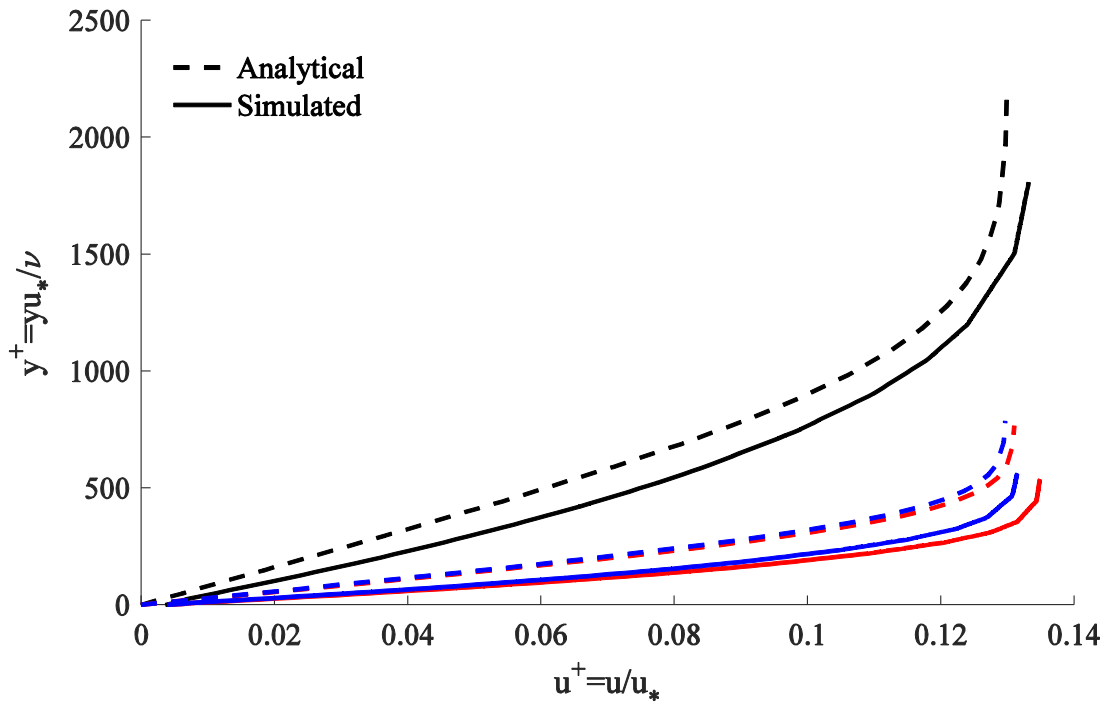


Figure 17: $x = 4R$ analytical and simulated velocity profiles for Power Law [16], Bingham Plastic [9], and Herschel-Bulkley fluid models

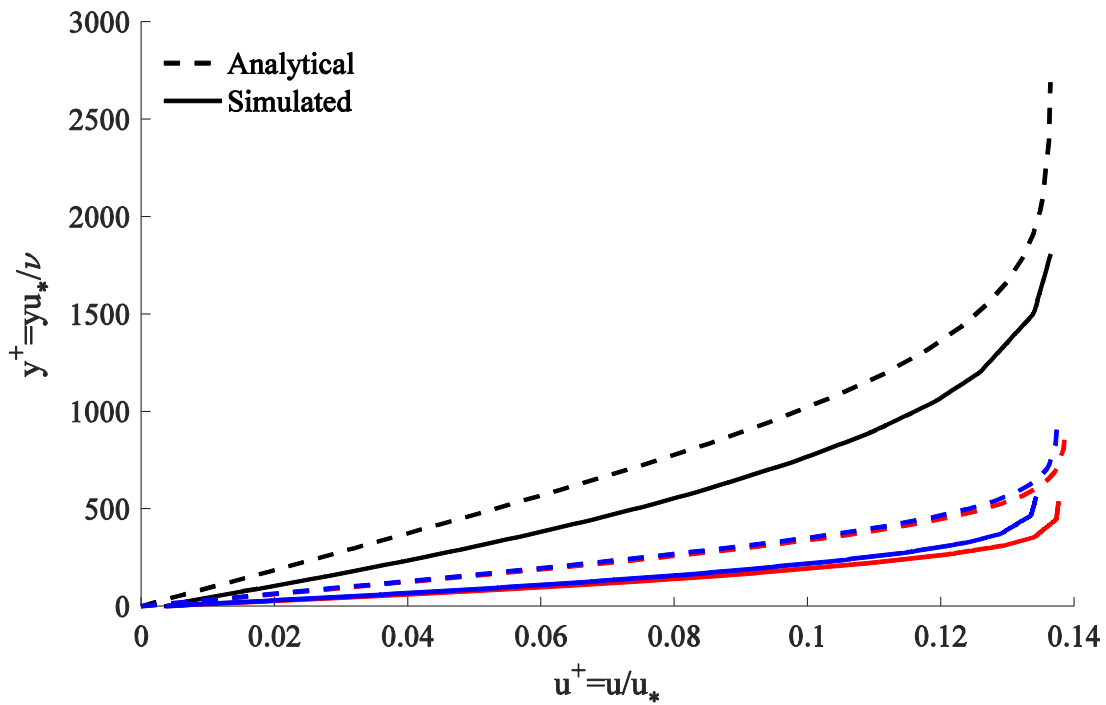


Figure 18: $x = 6R$ analytical and simulated velocity profiles for Power Law [16], Bingham Plastic [9], and Herschel-Bulkley fluid models

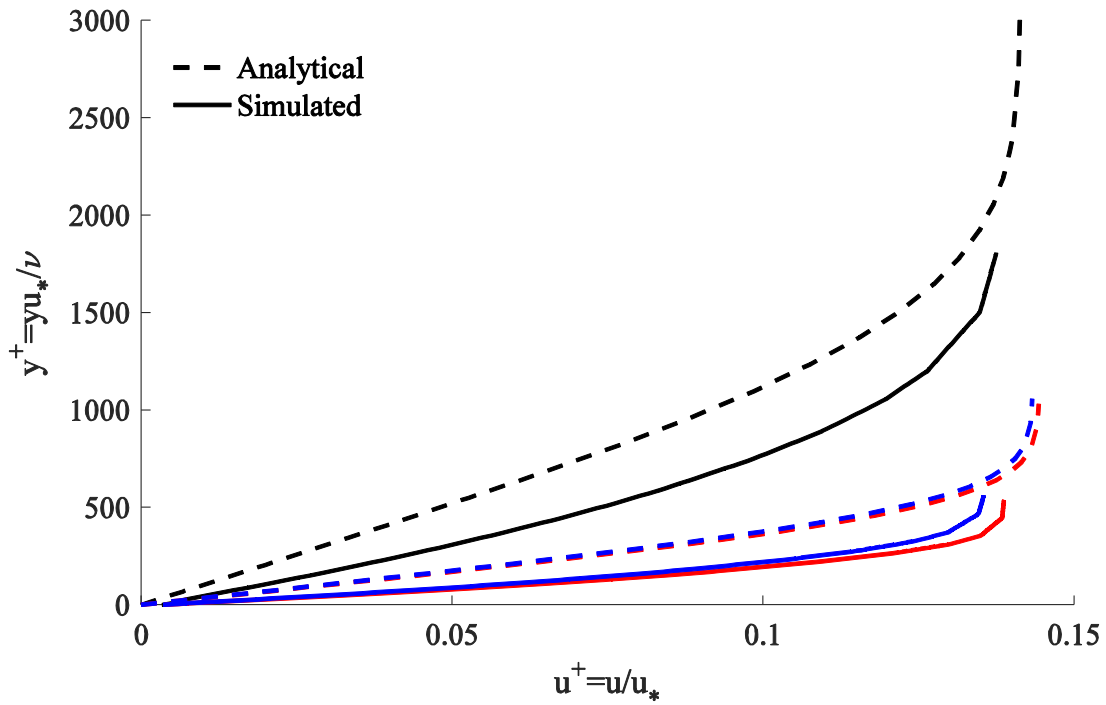


Figure 19: $x = 8R$ analytical and simulated velocity profiles for Power Law [16], Bingham Plastic [9], and Herschel-Bulkley fluid models

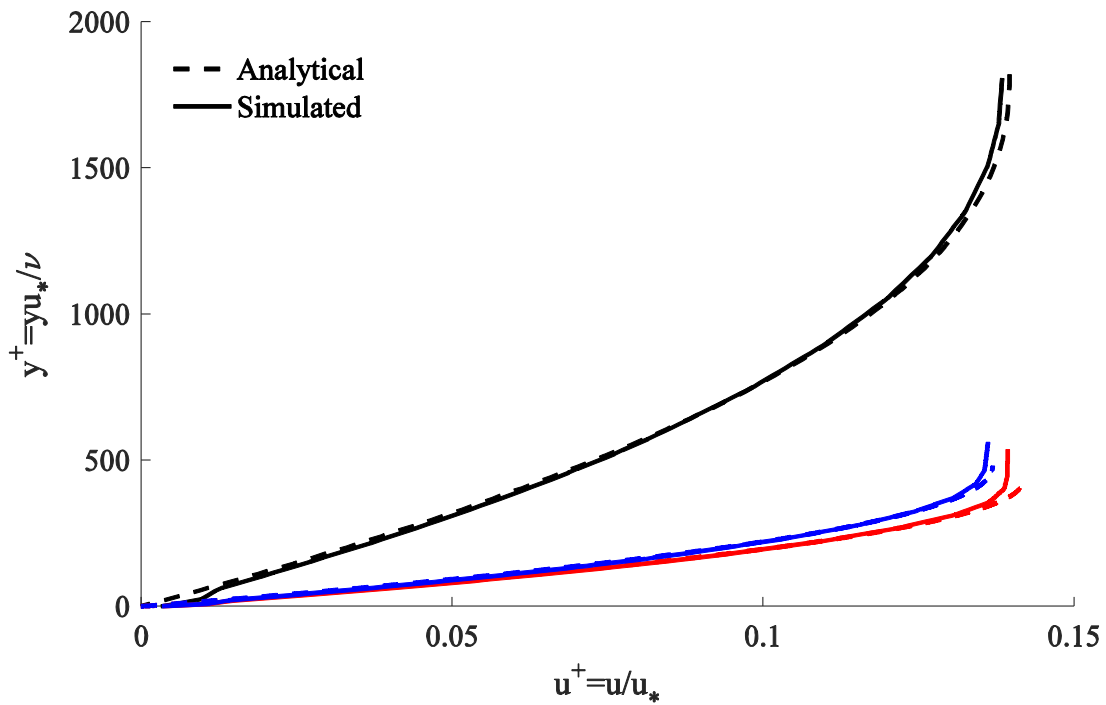


Figure 20: $x = 140R$ analytical and simulated velocity profiles for Power Law [9], Bingham Plastic [15], and Herschel-Bulkley [15] fluid models

The most noticeable difference in Figures 16-20 is how much further from the wall the Power Law model estimates the fluid velocity over either the Bingham Plastic or the Herschel-Bulkley fluid models. This is true even for the fully-developed velocity profiles shown in Figure 20 in which the Blasius solution does not apply. Another noteworthy characteristic difference is between the analytical solutions and the simulations within the entrance region. The analytical solutions have a consistently higher value from the wall for a given velocity over its simulated counterparts. This is not true for the fully-developed region in which the analytical result nearly overlaps the simulated results for each fluid model.

In the fully-developed region of the pipe the differential pressure, centerline velocity, entrance length, and wall shear stress, are found analytically and through simulation results. In the case of Herschel-Bulkley and Bingham Plastic fluid models the plug radius is also found. These are shown in the following Tables 9-11.

In addition to the flow parameters previously discussed and shown graphically for the Bingham Plastic flow model, the entrance length (L_{fd}) is found analytically using Equation (7) which is also valid for the other fluid models. (see Table 9)

In the case of the Power Law model, the flow rate and entrance velocity is preserved from the Bingham Plastic model parameters. Using Equations (10), (30), and (31) and the input coefficients from Table 4, the analytical values for the wall shear stress (τ_w), fully-developed velocity profile (τ_w), and pressure differential (dp/dx) are found, respectively. (see Table 10)

The same parameters are found for the Herschel-Bulkley model by using the input parameters located in Table 4. Equations (10), (27), and (35) are used to find the wall shear stress, differential pressure, and fully-developed velocity profile. The plug radius is a stipulation

for this flow model. These are shown together with the simulated results for the fully-developed parameters in Table 11.

Table 9: Bingham Plastic fully-developed results

<i>Analytical</i>	<i>Simulated</i>
$\delta P = 3695 \text{ Pa}$	$\delta P = 3460 \text{ Pa}$
$dp/dx = 2462 \text{ Pa/m}$	$dp/dx = 2471 \text{ Pa/m}$
$u(0) = 0.2868 \text{ m/s}$	$u(0) = 0.2865 \text{ m/s}$
$u_{fd} = 0.4973 \text{ m/s}$	$u_{fd} = 0.4903 \text{ m/s}$
$L_{fd} = 0.0992 \text{ m}$	$L_{fd} = 0.1395 \text{ m}$
$R_c = 0.0021 \text{ m}$	$R_c = 0.0027 \text{ m}$
$\tau_w = 12.3081 \text{ Pa}$	$\tau_w = 12.40 \text{ Pa}$

Table 10: Power Law fully-developed results

<i>Analytical</i>	<i>Simulated</i>
$dp/dx = 2949 \text{ Pa/m}$	$dp/dx = 2949 \text{ Pa/m}$
$u(0) = 0.2864 \text{ m/s}$	$u(0) = 0.2865 \text{ m/s}$
$u_{fd} = 0.5362 \text{ m/s}$	$u_{fd} = 0.5316 \text{ m/s}$
$L_{fd} = 0.0639 \text{ m}$	$L_{fd} = 0.0349 \text{ m}$
$\tau_w = 14.745 \text{ Pa}$	$\tau_w = 14.78 \text{ Pa}$

Table 11: Herschel-Bulkley fully-developed results

<i>Analytical</i>	<i>Simulated</i>
$\delta P = 3772 \text{ Pa}$	$\delta P = 3791 \text{ Pa}$
$dp/dx = 2694 \text{ Pa/m}$	$dp/dx = 2708 \text{ Pa/m}$
$u(0) = 0.2851 \text{ m/s}$	$u(0) = 0.2865 \text{ m/s}$
$u_{fd} = 0.5025 \text{ m/s}$	$u_{fd} = 0.4996 \text{ m/s}$
$L_{fd} = 0.0728 \text{ m}$	$L_{fd} = 0.1246 \text{ m}$
$R_c = 0.0015 \text{ m}$	$R_c = 0.0021 \text{ m}$
$\tau_w = 13.47 \text{ Pa}$	$\tau_w = 12.58 \text{ Pa}$

The Power Law fully-developed velocity profile does not have a critical plug radius as the Bingham Plastic model does. The Herschel-Bulkley plug radius is less than the Bingham Plastic plug radius indicating the blend of the Power Law model traits with those of the Bingham Plastic model.

The wall shear stress for all three cases have values close to each other. Another interesting find is the reduction in the entrance length for the Bingham Plastic and Herschel-Bulkley models compared to the Power Law model.

A similar process is completed for the non-Newtonian fluid models as was performed for the Newtonian fluid model to find the exponent, m , used in Equation (15). The exponent, m , is then used with the Blasius solution, Equation (14), for the Bingham Plastic and the Herschel-Bulkley fluid models. In the case of the Power Law fluid model, the centerline velocities found from the simulation are still used in the Blasius solution applied to the Power Law fluid model, Equation (33), where the value for the centerline velocity, u_c , is required. For the Power Law fluid model the pressure gradient is assumed to be zero. Figures 21-23 show the simulated centerline velocities and the curve fit. The analytical velocity profiles shown in Figures 16-19 are the result of this procedure.

The Punnis approximation to the centerline velocities are also shown on Figures 21-23. These are found from Equation (13) and are shown with a red x. The simulated centerline velocities are shown with blue circles and the curve fit is shown with a blue line.

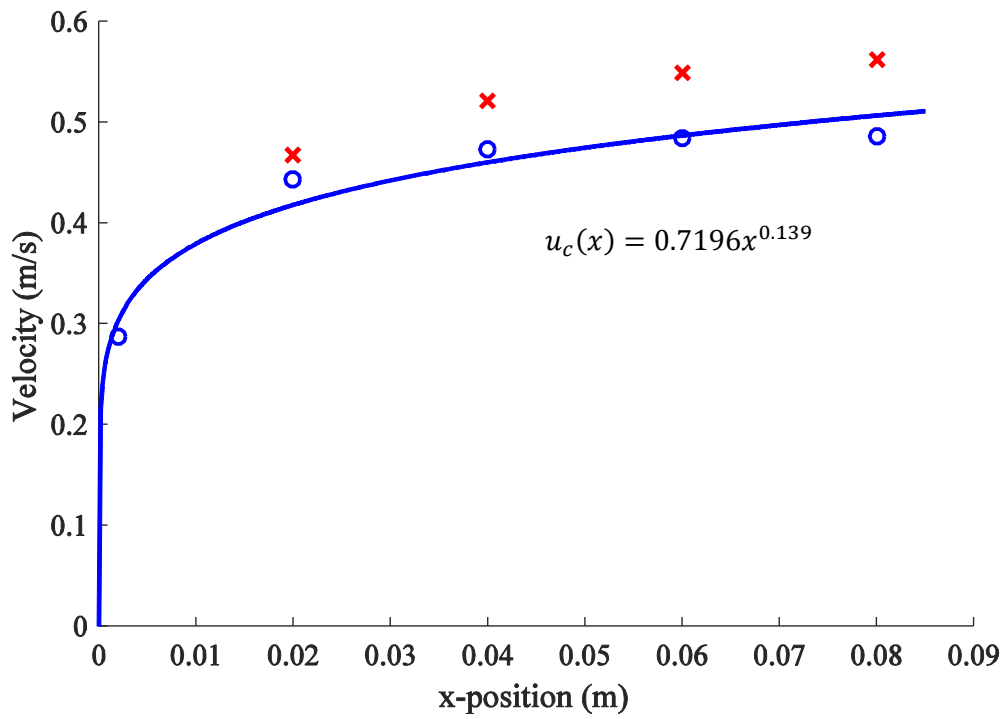


Figure 21: Bingham Plastic simulated centerline velocities with approximated centerline velocities [11]

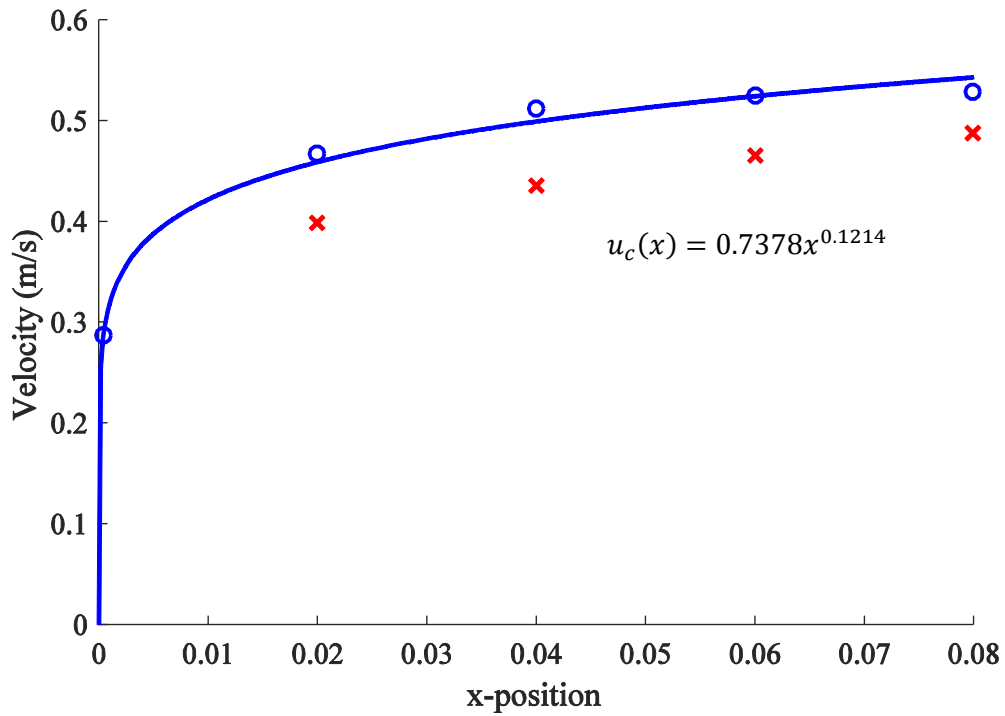


Figure 22: Power Law simulated centerline velocities with approximated centerline velocities [11]

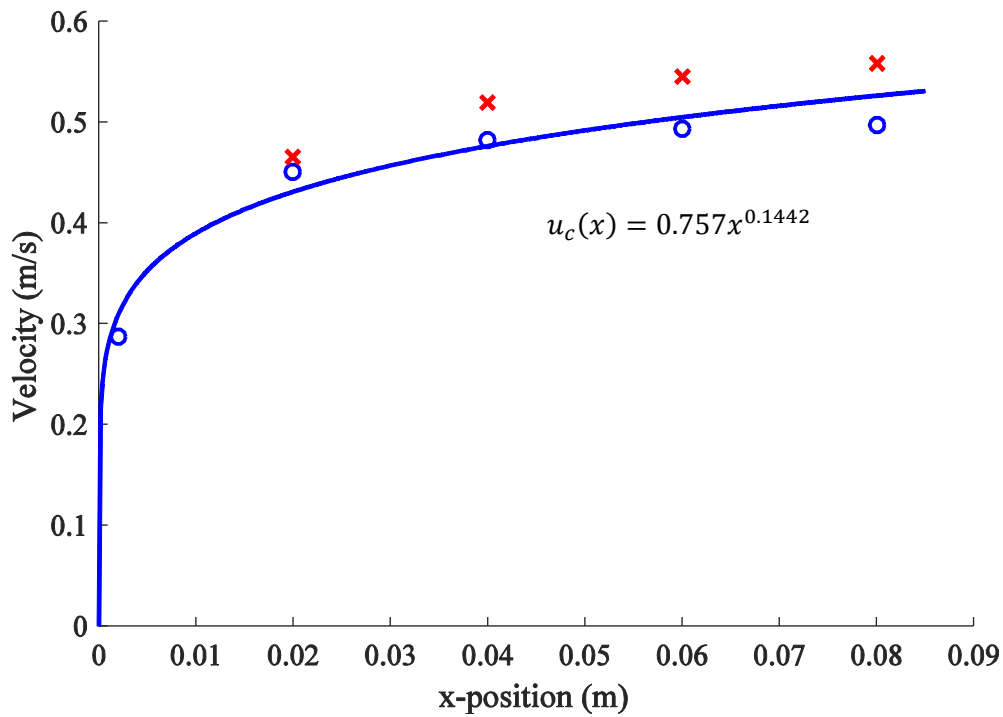


Figure 23: Herschel-Bulkley simulated centerline velocities with approximated centerline velocities [11]

The centerline velocities found through the approximation for all of the non-Newtonian fluid models are much closer to the simulated centerline velocities than those found for the Newtonian case. This is very interesting since the approximation was derived by Punnis [11] for Newtonian flows. In the case of the Herschel-Bulkley model, the centerline velocity approximation is quite similar to the Bingham Plastic fluid model. The results from Figure 23 are the closest to the simulated values of any of the fluid models presented in the thesis.

Another way of viewing the differences between the non-Newtonian fluid models is through non-dimensional velocity plots for each location along the pipe within the entrance region. In the plots, the velocity is on the y-axis and the distance is on the x-axis. The velocity as a function of radius for a particular location is made unit-less by dividing by the centerline velocity at that location or U/U_x . The distance, y , from the wall is divided by the boundary layer thickness, δ . For these plots, Figures 24-26, the same symbols and colors are used as in Figure 11.

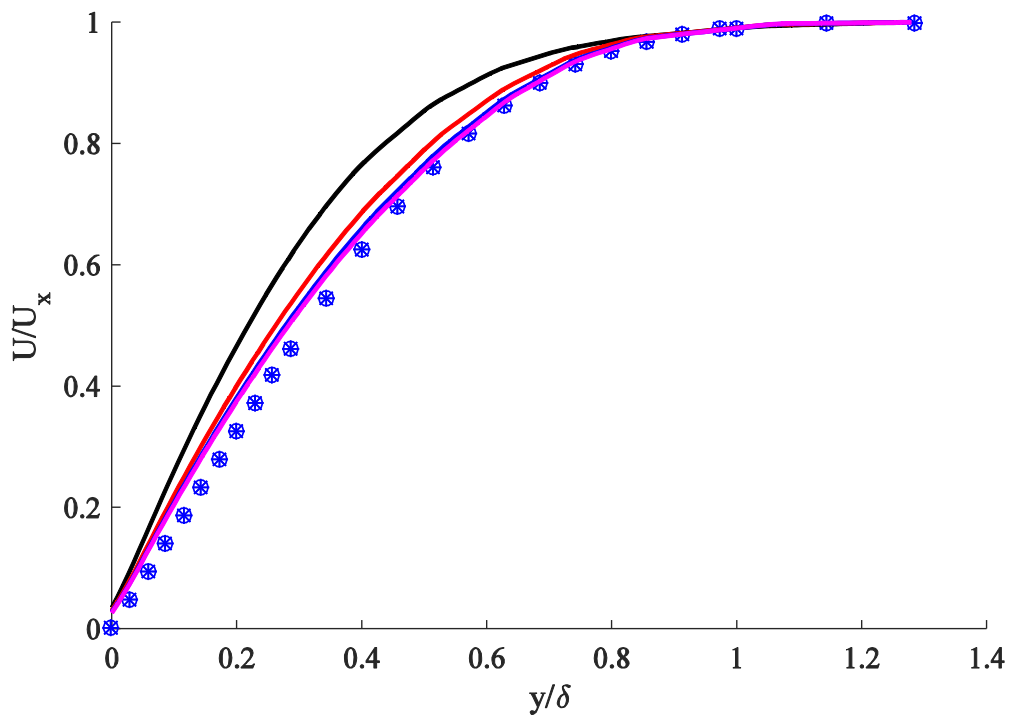


Figure 24: Non-dimensional analytical [9] and simulated Bingham plastic velocity profiles; for symbols: $x = 2R$ (o), $x = 4R$ (\times), $x = 6R$ (+), $x = 8R$ (*); for solid lines: $x = 2R$ (black), $x = 4R$ (red), $x = 6R$ (blue), $x = 8R$ (magenta)

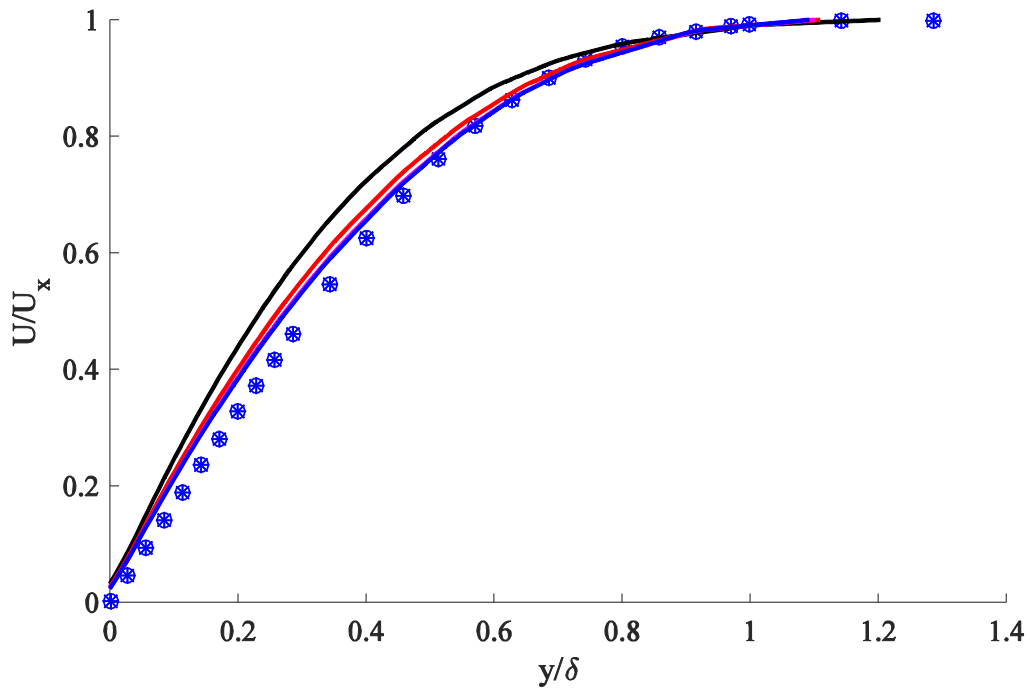


Figure 25: Non-dimensional analytical [16] and simulated Power Law velocity profiles; symbols and colors are the same as in Figure 24.

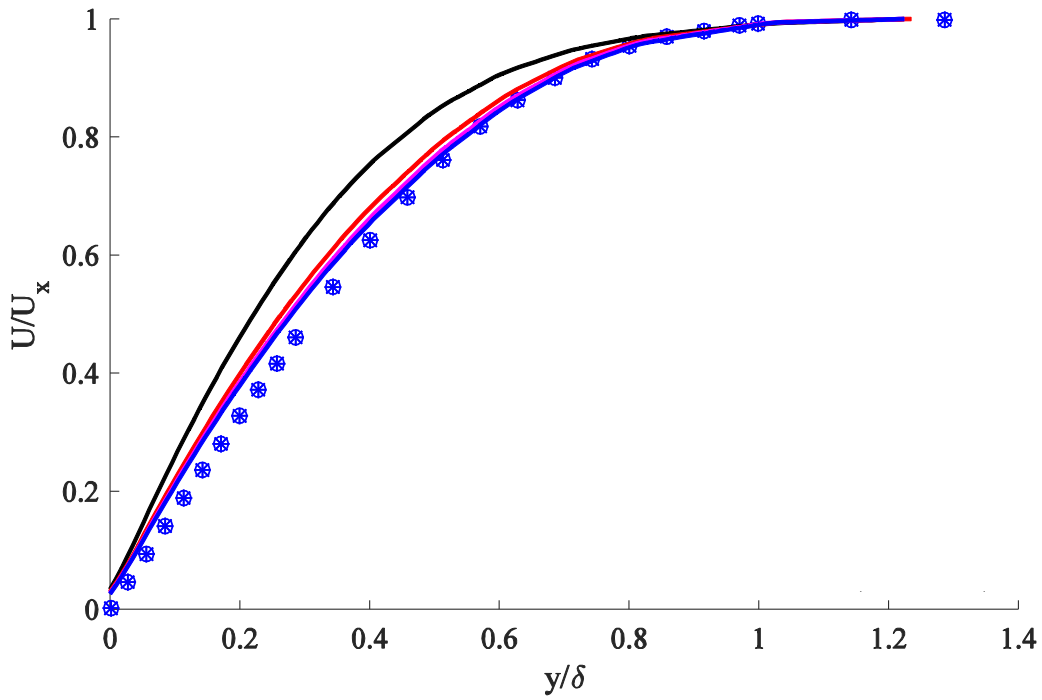


Figure 26: Herschel-Bulkley simulated and analytical [9] non-dimensional velocity profiles; symbols and colors are the same as in Figure 24.

In Figures 24-26 not many noticeable differences exist between the different fluid models. In all three cases the velocity profile at $x = 2R$ stands out from the otherwise mostly similar curves of the other locations. The most interesting feature of these plots is the similarity in the analytical non-dimensional velocity profiles. The Blasius solution applied to pipes is still similar even with a changing centerline velocity.

The result of this indicates that the Blasius solution only provides ball park estimates to the velocity profiles in the entrance region of a pipe. The differences between the analytical results and the simulated results could be attributed to the way in which the Blasius solution is used for the non-Newtonian fluid since the Blasius solution does allow the viscosity to be a parameter that changes. In reality, a plastic fluid, by definition, exhibits different effective viscosities for changes in shear rate. Since the plastic fluid has a velocity profile that is changing through the entrance length, it only makes sense that the Blasius approximation should take into account a viscosity value for each location. Even this is a simplification to the real phenomenon since the shear rate changes as a function of r as well as x in the entrance region. There are a range of effective viscosities for a given position along x that the viscosity is integrated over.

The subtle differences in Figures 24-26 are displayed directly by viewing the boundary layer thickness for each drilling fluid model. Figure 27 shows the boundary layer thickness for all three non-Newtonian fluid models together.

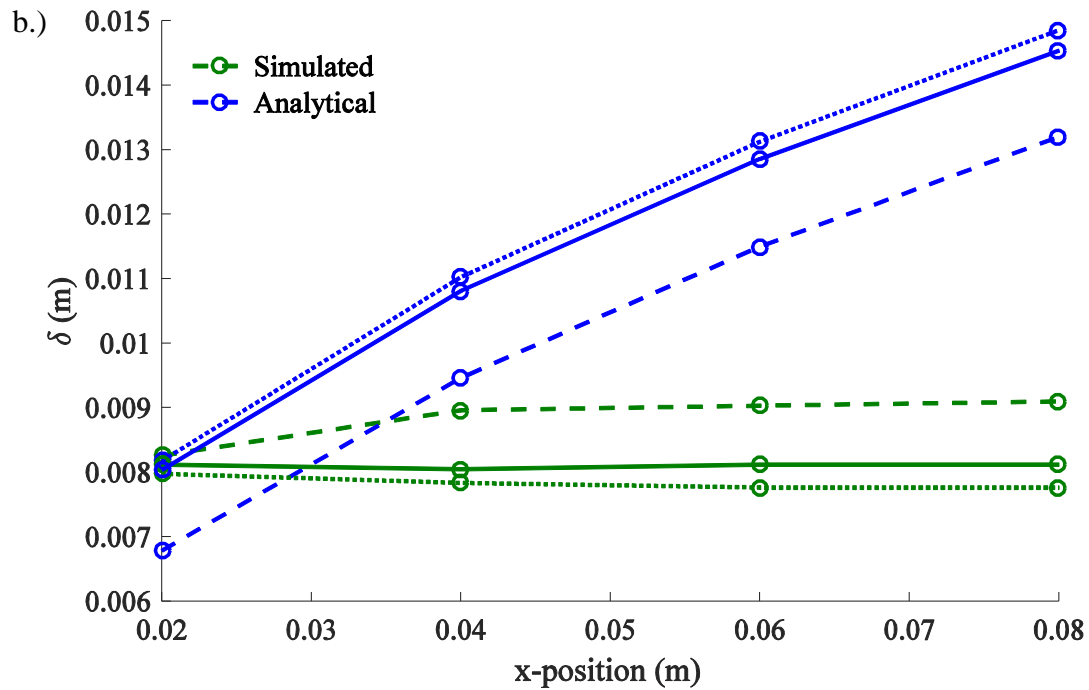
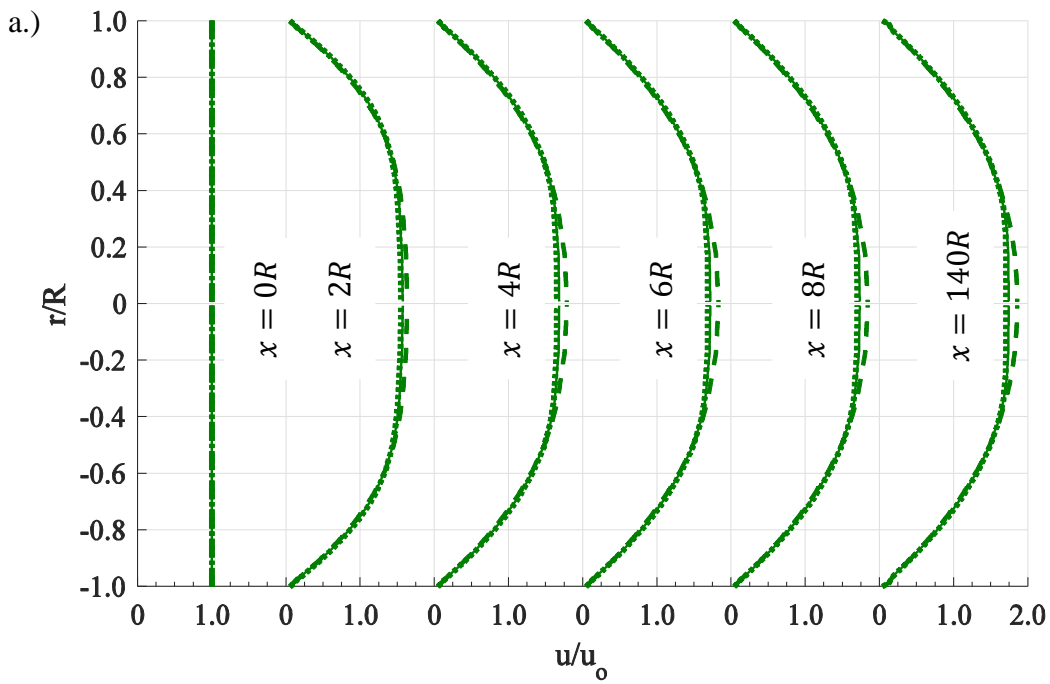


Figure 27: a.) Simulated velocity profiles and; b.) Boundary layer thickness comparison for all three non-Newtonian fluid types; Power Law (dashed lines), Bingham Plastic (dotted lines); Herschel-Bulkley (solid lines) [9]

For each fluid model in Figure 27 the simulations predict very small changes in the boundary layer thickness. The Power Law model is the only non-Newtonian model that predicts any growth in the boundary layer thickness. The values found for the Bingham Plastic and Herschel-Bulkley fluid models are very similar for either the simulated or the analytical results.

Another noticeable characteristic in Figure 27 is the drastic difference between the analytical solution and simulated results to the boundary layer thickness. Unlike the Newtonian model results for the boundary layer thickness, Figure 12, the analytical results and the simulated results do not agree in the way the boundary layer thickness changes as the fluid travels through the pipe. The boundary layer thickness is established to at least 90% of the maximum thickness within 2 pipe diameters in any of the simulations.

CONCLUSIONS

The simulated results for the Newtonian fluid model using Star-CCM+ and Solidworks Flow Simulation are nearly identical and compare well with the analytical solutions. Both meshes produced accurate results as seen by the convergence plots and the velocity profiles in the entrance region as well as the fully-developed flow parameters. The same is true for the extended pipe case in which the velocity profiles neatly matched those for the shorter pipe with the simulations performed in Solidworks. The results of the Newtonian fluid model provided a mesh and validated the Solidworks software.

It was shown that the analytical solutions with the pressure gradient used in the Newtonian fluid model came closer to the simulated results than the analytical solutions without a pressure gradient. For pipe flow, it is clear that a solution utilizing the pressure gradient should be used.

In all cases, except at $x = 2R$ for the Power Law fluid model, the analytical velocity profiles within the entrance region predicted larger values of distance from the pipe wall, y^+ , for a given velocity, u^+ . The reason for these differences could be attributed to the pipe diameter to boundary layer thickness ratio. It is seen that the boundary layer thickness found analytically increases to a thickness greater than the radius of the pipe. If a greater velocity were chosen then the boundary layer thickness would decrease and the Blasius solution would have provided a closer approximation to the simulated results. The same would have occurred if a larger pipe diameter was used for the inlet velocity specified.

The fully-developed velocity profiles and the flow parameters (wall shear stress, pressure differential, and plug radius) were closely matched for the simulated and analytical results. The

pipe entrance length did have some significant differences which are not explained. Otherwise the analytical Herschel-Bulkley fluid model provided accurate results without the aide of expensive CFD analysis.

The Punnis approximation to the centerline velocities in the entrance region of the pipe were surprisingly close to the simulated values. In fact the smallest difference between the analytical and simulated centerline velocities occurred in the Herschel-Bulkley fluid model. Perhaps the Punnis approximation can be used with the Blasius solution to find accurate velocity profiles in the entrance region of a pipe if the ratio between the pipe diameter and the boundary layer thickness is large.

Of the simulated results, both the Bingham Plastic and the Herschel-Bulkley fluid models are in agreement with the theory behind the reasons for choosing non-Newtonian fluids as drilling fluids. Specifically, the shear-thinning characteristic is favorable in drilling fluids since shear velocity in the fluid plug is very low which correlates with a high effective viscosity. It is this highly viscous fluid plug that is largely responsible for cuttings transport. Another favorable characteristic is the high shear rate within the fluid layer that is the boundary layer. The high shear rate within the boundary layer produces relatively low effective viscosity and shear stress. Both Bingham Plastic and Herschel-Bulkley fluid models predict this, but it is the Herschel-Bulkley model that more closely follows the data obtained from the Fann meter. Thus, the Herschel-Bulkley model is more accurate and, with computational ability, will provide cost savings for drillers.

REFERENCES

- [1] Drilling Fluids Processing Handbook, Amsterdam: Gulf Professional Pub., 2005.
- [2] Chevron, "PV, YP, and Tau Zero; One of These Properties Is Not Like The Others," *Fluids & Waste Management News Digest*, pp. Volume 6, Issue 1, pgs. 1-4, 2010.
- [3] R. B. Winslow H. Herschel, "Konsistenzmessungen von Gummi-Benzollösungen," *Kolloid-Zeitschrift*, Volume 39, Number 4, p. 291, 1926.
- [4] "Properties of Fluid," [Online]. [Accessed 30 July 2015].
- [5] Dassault Systems, [Online]. Available: <http://www.solidworks.com/sw/products/simulation/flow-simulation.htm>. [Accessed 15 August 2016].
- [6] CD-adapco, [Online]. Available: <http://www.cd-adapco.com/products/star-ccm%C2%AE>. [Accessed 15 August 2016].
- [7] I. Currie, *Fundamental Mechanics of Fluids*, Boca Raton, FL 33487: CRC Press, 2013.
- [8] R. K. Shah and A. L. London, "Laminar Flow Forced Convection in Ducts," *Advances in Heat Transfer*, vol. 1, 1978.
- [9] J. A. Schetz, *Boundary Layer Analysis*, Reston, VA: American Institute of Aeronautics and Astronautics, 2011.
- [10] H. Schlichting, *Boundary Layer Theory*, New York: McGraw-Hill, 1955.
- [11] B. Punnis, "Zur Berechnung Der Laminaren Einlaufstromung Im Rohr," Gottingen: n.p., 1947.
- [12] V. M. Falkner and S. W. Skan, "Some Approximate Solutions of the Boundary Layer Equations," in *Aeronautical Research Council, ARC R&M 1314*, London, 1930.
- [13] H. Darley, *Composition and Properties of Drilling and Completion Fluids*, Houston: Gulf Pub., Book Division, 1988.
- [14] R. W. Hanks, "On the Flow of Bingham Plastic Slurries in Pipes and Between Parallel Plates," *Society of Petroleum Engineers Journal* 7.04, pp. 342-46, 1967.

- [15] J. F. Steffe, *Rheological Methods in Food Process Engineering* 2nd ed., East Lansing, MI: Freeman, 1992.
- [16] A. Acrivos, "Momentum and Heat Transfer in Laminar Boundary-Layer Flows of Non-Newtonian Fluids Past External Surfaces," *AIChE Journal* 6.2, pp. 312-17, 1960.
- [17] N. Cheremisinoff, "Editor," in *Encyclopedia of Fluid Mechanics: Slurry Flow Technology*, Vol. 5, Houston, TX, Gulf Pub. Co., 1986.
- [18] K. El-Nahhas, "Flow Behaviour of Non-Newtonian Clay Slurries," in *Ninth International Water Technology Conference, IWTC9*, Sharm El-Sheikh, Egypt, 2005.
- [19] Y. A. Cengel, in *Heat and Mass Transfer: Fundamentals & Applications 4th ed.*, New York, McGraw-Hill, 2011, p. 878.
- [20] R. C. Gupta, "Laminar Entrance Region Flow of Herschel-Bulkley Fluids in a Circular Pipe," *Journal of Polymer Engineering*, p. 22.3, 2002.
- [21] G. Batchelor, *An Introduction to Fluid Dynamics*, Cambridge: U.P., 1967.
- [22] "Drilling Fluids Reference Manual," [Online]. [Accessed 29 July 2015].
- [23] "Boundary Layer Flow of Reiner-Philippoff Fluids," *International Journal of Non-Linear Mechanics*, pp. 871-77, 1994.
- [24] F. M. White, "Laminar Boundary Layers," in *Viscous Fluid Flow 3rd ed.*, New York, NY, McGraw-Hill Higher Education, 2006, p. 215+.
- [25] H. Blasius, "Boundary Layers in Fluids with Small Viscosity," *Zeitschrift fur angewandete Mathematik und Physik*, vol. 56, no. 1, pp. 1-37, 1908.